

Review

Recent Studies on Multifunctional Electrocatalysts for Fuel Cell by Various Nanomaterials

Sanha Jang [†], Kyeongmin Moon [†], Youchang Park, Sujung Park and Kang Hyun Park ^{*†} 

Department of Chemistry, Pusan National University, Busandaehak-ro 63beon-gil, Geumjeong-gu, Busan 46241, Korea; jangs0522@naver.com (S.J.); moonkm205@naver.com (K.M.); changi3356@nate.com (Y.P.); llopoby@gmail.com (S.P.)

* Correspondence: chemistry@pusan.ac.kr; Tel.: +82-51-510-2238

[†] These authors contributed equally to this work.

Received: 14 May 2020; Accepted: 2 June 2020; Published: 3 June 2020



Abstract: Based on nanotechnology, nanocomposites are synthesized using nanoparticles (NP), which have some advantages in terms of multifunctional, economic, and environmental factors. In this review, we discuss the inorganic applications as well as catalytic applications of NPs. Recently, structural defects, heteroatomic doping, and heterostructures of such efficient ideal catalysts and their application as multifunctional catalysts for hydrogen evolution reaction (HER) and oxygen evolution reaction (OER) in water splitting. It has been verified that the catalysts used in oxygen reduction reaction and OER can be used effectively in metal/air batteries. Moreover, it has been reported that high-efficiency catalysts are required to implement urea oxidation reaction (UOR), which involves a six-electron reaction, as an electrochemical reaction. We expect that this review can be applied to sustainable and diverse electrochemistry fields.

Keywords: multifunctional catalyst; water splitting; hybrid nanoparticle; electrochemistry; oxygen reduction reaction; oxygen evolution reaction; hydrogen evolution reaction; urea oxidation reaction

1. Introduction

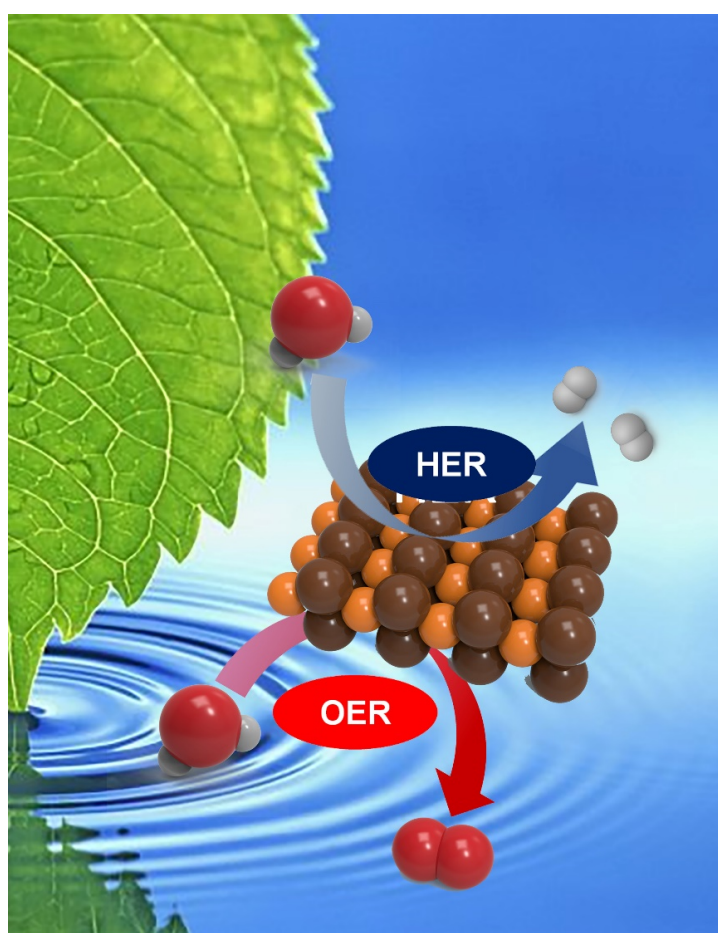
A material comprising two or more constituents is generally referred to as a hybrid material (Scheme 1). Such a hybrid material not only has the unique characteristics of each individual component, but also has additional synergistic characteristics [1–3]. Such synergistic characteristics allow their application as catalysts and sensors, as well as for adsorption, desorption, etc., [4]. Because of properties like high selectivity for a particular material, high catalytic efficiency, and high physical/chemical stability compared to catalysts based on one metal, multimetallic fusion nanoparticles (NPs) have been synthesized for use as catalysts in recent years [5–14]. The synthesis of such multicomponent nanostructures with improved functionalities has been explored by many researchers [15–25].



Scheme 1. Schematic diagram of hybrid metal nanoparticles (NPs) from monometallic NPs.

The realization of a hydrogen-based, renewable, and sustainable energy cycle offers a clear vision to secure resources for our upcoming future. High-performance electrode catalysts for power conversion systems like fuel cells and water splitting reactions are central to this thrust [26–29].

Hydrogen-producing electrochemical water splitting is a promising technique for renewable energy production and storage [30,31]. In fact, owing to its potential for substituting fossil fuels, the electrochemical conversion of H_2O into hydrogen fuel ($2\text{H}_2\text{O} \rightarrow 2\text{H}_2 + \text{O}_2$) has been successfully achieved (Scheme 2). The water splitting method usually involves two-half processes. One process is the anodic oxygen evolution reaction (OER), and the other is the cathodic hydrogen evolution reaction (HER) [32]. There are literature reviews that show that several electrocatalytic systems for water splitting have been reported with many different elementary formulations and microstructures [33–36]. With the increased use of wide-throughput combinatorial methods for the development of new OER and HER catalysts in various ternary and quaternary structure spaces, this number is likely to increase rapidly in the future [37–43].



Scheme 2. Illustration of hydrogen evolution reaction (HER) and oxygen evolution reaction (OER) activity in water electrolysis.

HER and OER performance can be enhanced based on three aspects (Scheme 3):

- Defect sites
- Heteroatoms
- Heterostructures

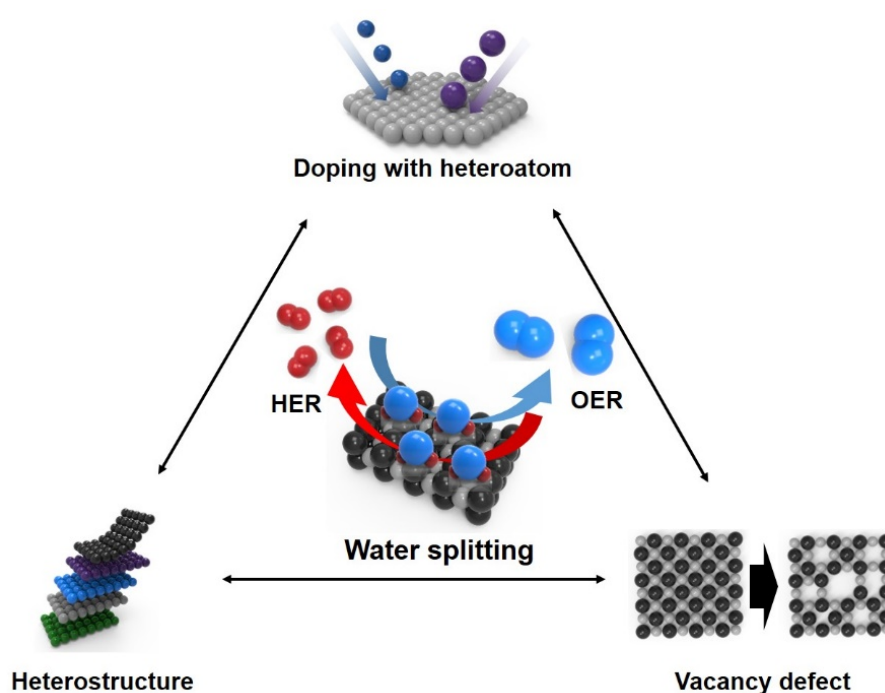
Hitherto, surface defect development approaches appear promising for the achievement of high-performance HER electrocatalysis owing to their tunable electrical properties [44–46]. Nonetheless,

while the quantity of edge sites in the nanostructure increases the HER efficiency, the manufacturing process limits the efficiency [47]. Edge sites enhance the activity by increasing the surface of the catalyst. A common technique involves the design and development of porous, hollow micro, and nanostructured electrocatalysts with a large number of catalytically active sites, reduced weight, and load transportation diffusion [48,49]. This may also lead to the development of the reactivity of the active sites by adding oxygen vacancies, resulting in major improvement in electrocatalytic operations [45].

Over the past decades, a number of earth-abundant metal-based composite materials, including oxides, chalcogenides, nitrides, borides, and phosphides, have been used to catalyze both the HER and OER [50–59]. Because of their hydrogenase-like catalytic mechanism in the HER and partial creation of active metal oxyhydroxides in the OER, transition metal phosphide (TMP)-based materials demonstrate noteworthy HER and OER activities among these well-explored electrocatalysts [60–63].

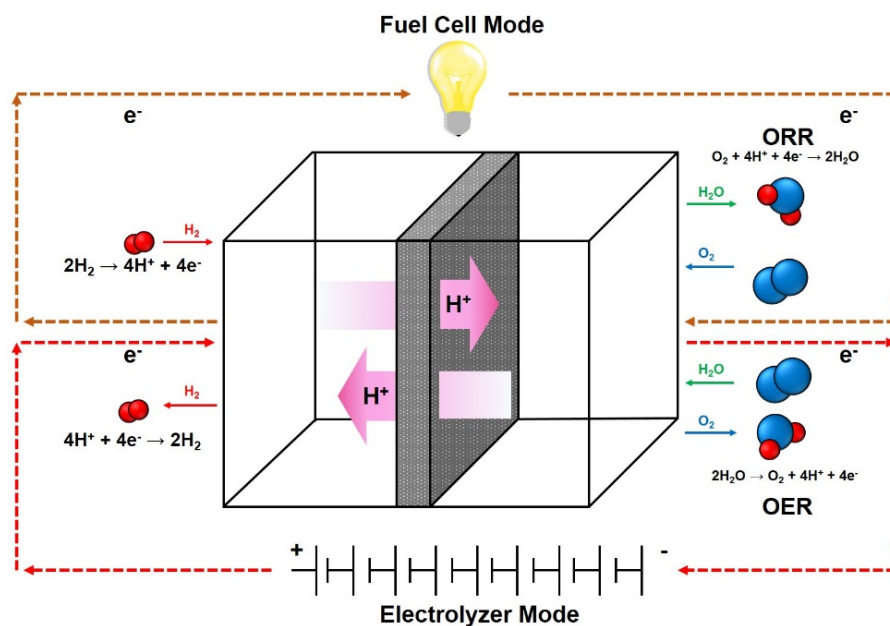
Heteroatom-doping is an effective method for further electrocatalyst activity enhancing by regulating the electronic structure, increasing the number of active sites, and maximizing intermediate formation capacity. In addition, co-doping of binary or ternary heteroatom catalysts can optimize catalytic activity with respect to their single-doped counterparts via synergistic coupling [64].

The heterostructured catalyst comprises two or more kinds of materials, typically bound together physically or chemically. Recently, an attractive variety of heterostructured catalysts were identified, demonstrating exceptional catalytic efficiency against electrochemical water splitting equivalents [65–69]. Most heterostructured catalysts exhibit higher HER behavior than their single-structured counterparts because of the many advantages of the former. Several heterostructured catalysts demonstrate high-quality HER activity over a broad pH spectrum and/or multifunctional HER and OER activity [70].



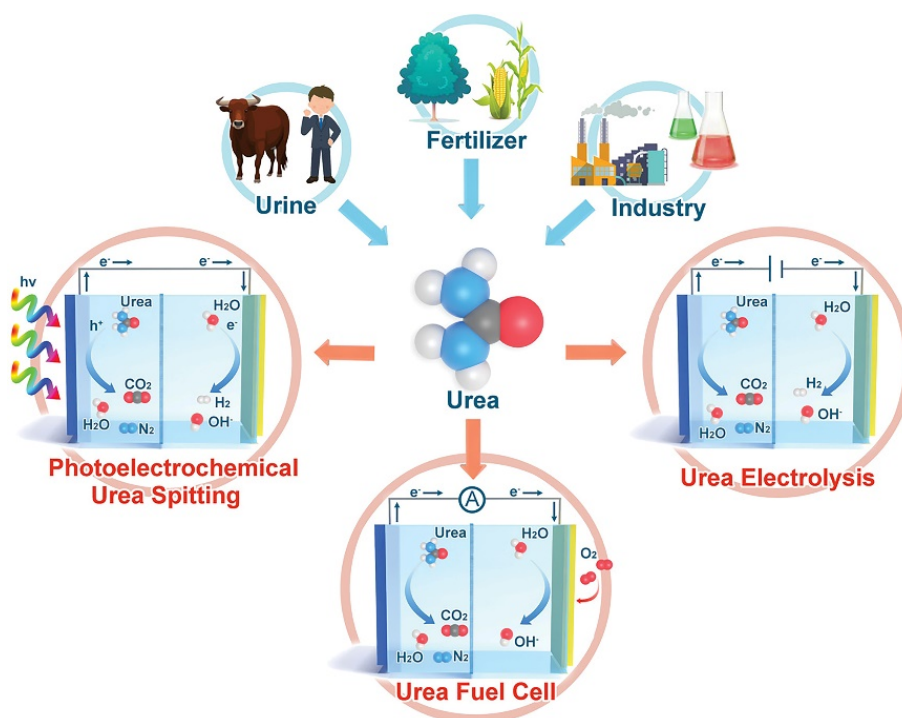
Scheme 3. Various methods of improve efficiency in water splitting.

The oxygen reduction reaction (ORR) and OER are emerging as highly relevant electrochemical reactions owing to the growing emphasis on renewable power generation technologies (Scheme 4) [27,71]. Lithium-oxygen batteries (LOBs) having the extremely high theoretical energy capacity have drawn significant attention in recent years [72,73].



Scheme 4. Schematic image of oxygen reduction reaction (ORR) and OER battery.

The international research community has recently reported that advanced manufacturing studies, such as transformation from a coal-based system to a H₂-based one for effective power storage and sewage disposal will offset many emerging advances in energy and environmental pollutant technologies (Scheme 5) [74,75]. Among the various recently established energy storage electrolysis technologies, urea electrolysis is remarkably intriguing, allowing the simultaneous disposal of urea-rich wastewater through the oxidation of the urea and a healthy, environmentally sustainable mass processing of H₂ fuel [76].



Scheme 5. Illustration of energy conversion technologies based on urea. Reproduced and adapted from Ref. [77]; Copyright (2020), Wiley.

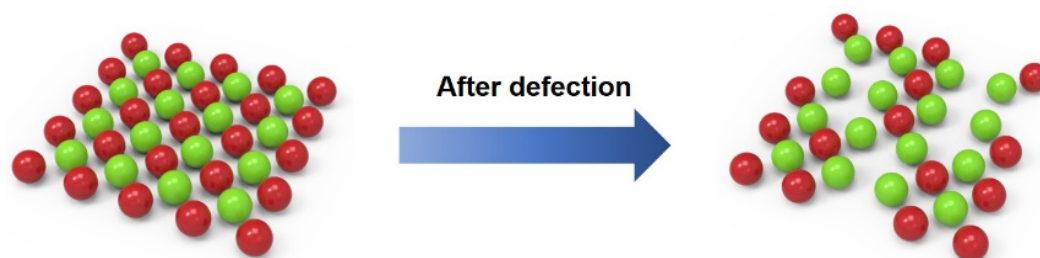
In this review, we focus on multifunctional nanomaterials and nanocomposites and their modifications in different fields:

- Interesting means to increase water splitting in hydrogen and oxygen evolution reactions, such as defect sites, doping of heteroatoms, and heterostructures.
- Fuel cell technology using ORR and OER.
- Specific electronic processing with urea decomposition to address environmental problems.

2. Methods of Increasing Water Splitting in HER and OER

2.1. Defect Sites

In case of vacancy defects, one part of the lattice becomes deficient and unstable, thereby enhancing activity with the reactive species [78]. Various defects have been established in NPs such as vacancies and lattice defects. Thus, catalysts with defect sites in their lattice provide more active sites, and consequently, greater reactivity than defect-less catalysts with the same surface area (Scheme 6). In particular, catalysts that intentionally create coalesced defect sites can further enhance the rate of chemical reactions, because the deficiency of the lattice effectively lowers the hydrogen adsorption energy and hydrogen diffusion energy barriers in HER, which are significant for the overall rate of water decomposition [79,80]. In addition, the electrochemical activity of the catalyst should be enhanced by introducing chalcogen into the defective sites, as suggested by the increase in reactivity of the active sites for HER and OER based on the defect sites of oxygen atom [81–84]. The existing methods of composing defect sites are ball milling, plasma technology, etching, etc. Ball milling is the process of grinding matter in ball mill and turning it into fine powder, and this is the relative adjustment of anti-site defect and vacancies in crystal. The plasma technology is mainly carried out in vacuum chamber, then is applied to gas or electric field to generate plasma after air enters the chamber. From this plasma, the energy of ions often determines defect density. The plasma technology can obtain vacancy defects on a constant basis. Li's group explain making defect sites through etching method.



Scheme 6. Schematic diagram for achieving defect sites of lattice.

2.1.1. Tafel Reaction of MoSe₂ through Coalesced Vacancies

A recent study by Li et al. suggested that the sulfur vacancies and tensile strength in molybdenum disulfides can trigger the basal plane with optimization the free energy difference associated with HER [85]. The formation of defect sites has been proven to enhance the HER operation by electrochemical methods, hydrogen annealing, and etching by plasma [85–87]. Based on these findings, in this research, the in-situ defect site in MoSe₂ has been established via hydrogen reactivity control during the chemical vapor deposition (CVD) process. The vacancy-controlled MoSe₂ exhibited outstanding HER behavior, reflected by an unprecedented Tafel reaction. In addition, when MoSe₂ has been synthesized in hydrogen and Ar atmospheres as carrier gases, the density of Se vacancies is significantly affected by the concentration of these carrier gases. They can serve either as a reactivity booster by promoting the substitution of MoO₃ and Se or as an etching substance for Se atoms in MoSe₂, leading to vacancy-controlled MoSe₂ [88,89].

Scheme 7 illustrates a synthesis mechanism for MoSe₂-X, in which X refers to the relative concentration of H₂ in the carrier gas (X = 0, 10, 20, 30, 40, and 50). During the growth process, the vacancy of Se was controlled by regulating the concentration of H₂ gas for CVD, as follows:

- Reducing stable MoO₃ to reactive MoO_{3-x} to improve the activity between Se and metal oxides under hydrogen assistance.
- Selenization of MoO_{3-x} to MoSe₂ via the substitution reaction of Se and O.
- Use of the substrate for nucleation and growth of MoSe₂.
- Etching of Se atoms in MoSe₂ by generating H₂Se gas under hydrogen assistance.



Scheme 7. Schematic illustration for growth and synthesize Se-vacancy controlled MoSe₂ with H₂ concentration control. H₂ plays a dual role in enhancing the reduction of MoO₃ (decreased vacancies) and Se etching at the MoSe₂ lattice (decreased vacancies). Reproduced and adapted from Ref. [79]; Copyright (2019), Elsevier.

In the growth procedure for MoSe₂, hydrogen has significant impact on the etching of Se atoms in MoSe₂ (increase in the density of Se vacancies) and on the reduction of MoO₃ (reduction in the density of Se vacancies) [88,89]. MoO₃ is not completely reduced at low H₂ concentration, and MoO_{3-x} impurities are produced by the low activity of Se and MoO₃ (MoSe₂-10). On the other hand, relatively high concentrations of H₂ gas (MoSe₂-30 and MoSe₂-50) facilitates the reaction between Se and MoO₃, which inhibits the accumulation of MoO_{3-x} impurities.

In the presence of H₂ gas, the creation of Se vacancies in MoSe₂ from pristine MoSe₂ are illustrated in Figure 1a. Annular dark-field-scanning transmission electron microscopy (ADF-STEM) images (Figure 1b) show that MoSe₂-30 was synthesized as hexagonal MoSe₂ with minimum Se vacancies. However, in MoSe₂-50, which was also synthesized as a hexagonal structure with high crystallinity, vacant Se sites were observed more frequently than in MoSe₂-30. Further, these vacancy sites were generally formed close to each other, resulting in the formation of coalesced vacancies. The single-Se vacancy sites of Se atoms were described using the mapping of the atomic location depicted in Figure 1c, caused predominantly by the etching of hydrogen.

After dropping vacancy-controlled MoSe₂-X materials onto a glassy carbon electrode without using polymeric binding agents, the monolayer's HER activities were investigated in 0.5 M H₂SO₄ electrolyte by using a three-electrode framework based on linear sweep voltammetry (LSV) curves (Figure 2a) and Tafel slopes obtained from polarization curves (Figure 2b). The Pt/C polarization curve indicates standard hydrogen production with an onset potential near approximately 0 V vs. RHE and a significantly rising current density. As reported in previous literature, the Tafel slope of Pt/C was 30 mV dec⁻¹, which means that Pt/C follows a Volmer–Tafel mechanism in its HER pathway [90]. For the monolayer electrocatalysts MoSe₂-X, the sum of Se vacancies in the MoSe₂ lattice is nearly in agreement with the HER activities. Owing to less number of vacancies, MoSe₂-30 displayed the lowest HER efficiency with an onset potential of -0.3 V and a gradually rising current density. Although MoSe₂-10 contains a large number of vacancies in the MoSe₂ lattice, it demonstrates only modest electrochemical performance, possibly owing to the large number of MoO_{3-x} impurities present on the surface of the catalyst, interfering with the transition of the carrier needed for the development of

hydrogen. Conversely, a dramatic enhancement in HER behavior was observed for MoSe₂-50, with a more positive onset potential close to -0.16 V, and a rapidly increasing current density such as in Pt/C. Interestingly, MoSe₂-50 with the clean surface exhibited a quite low Tafel slope (33 mV dec⁻¹), close to the onset potential owing to the coalesced vacancies. Further, unlike the typical trend of Tafel plots in transition metal dichalcogenide (TMDs), which increases significantly with increasing voltage, the Tafel plot of MoSe₂-50 was retained almost at the same level as 33 mV dec⁻¹ in the high-overpotential area as well. The slope of this Tafel plot is among the smallest recorded to date, including TMDs of the 1T and 2H level, quite similar to that for Pt/C [85–87,91–94]. The HER performance of intermediate samples (MoSe₂-20 and MoSe₂-40) are also depicted in Figure 2c. By decline of MoO_{3-x} group in MoSe₂-20, improved HER performance was triggered compared to MoSe₂-10, leading to a lower Tafel slope. The HER activity in MoSe₂-40 suggests intermediates between MoSe₂-30 and MoSe₂-50, primarily owing to less number of active sites than MoSe₂-50.

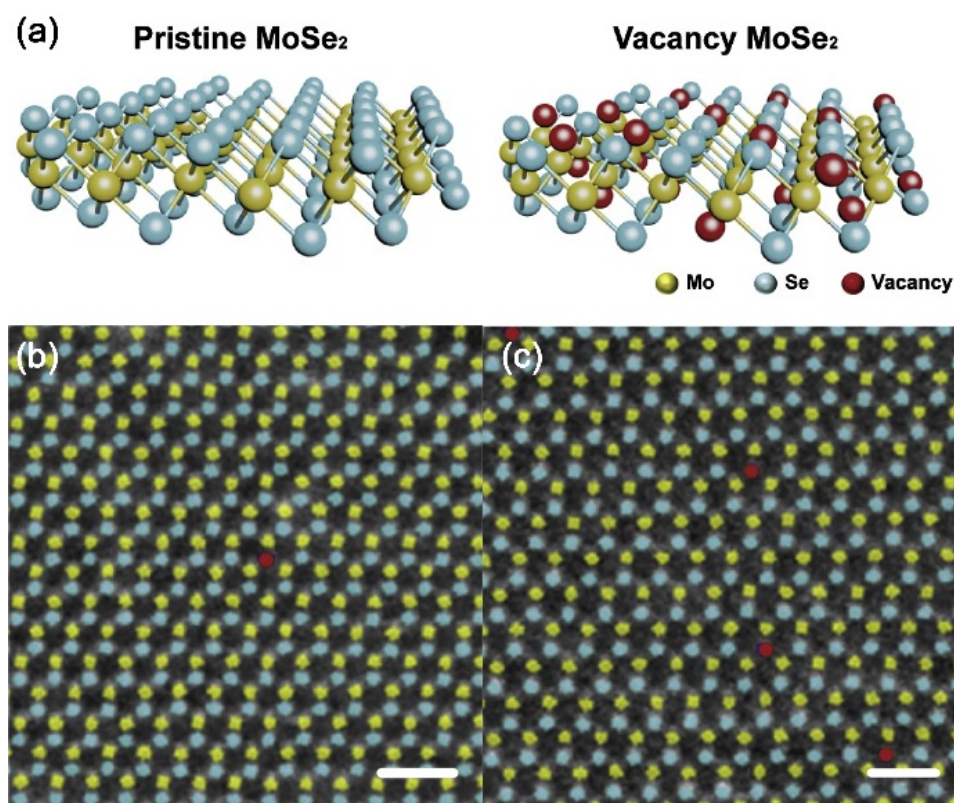


Figure 1. (a) Schematic diagram of lattice structure change in vacancy-MoSe₂. Atomic-resolution annular dark-field-scanning transmission electron microscopy (ADF-STEM) position mapping image of (b) MoSe₂-30 and (c) MoSe₂-50. The bars indicate (b) and (c) 1 nm. Reproduced and adapted from Ref. [79]; Copyright (2019), Elsevier.

The typical HER in TMDs mostly follows the Heyrovsky mechanism, which requires an extra electron transfer to adsorbed hydrogen on a catalytic surface (H^*) to generate H_2 ($H^* + H^+ + e^- \rightarrow H_2$). In comparison, the extremely low and steady Tafel slope with a large overpotential for MoSe₂-50 is most likely caused by the Tafel reaction, in which only two H^* must be combined to generate H_2 without any extra electron transfer ($H^* + H^* \rightarrow H_2$). Thus, high HER performance in vacancy-induced MoSe₂ relates to the extra Tafel reaction because of the creation of coalesced Se vacancies, as depicted in Figure 2c.

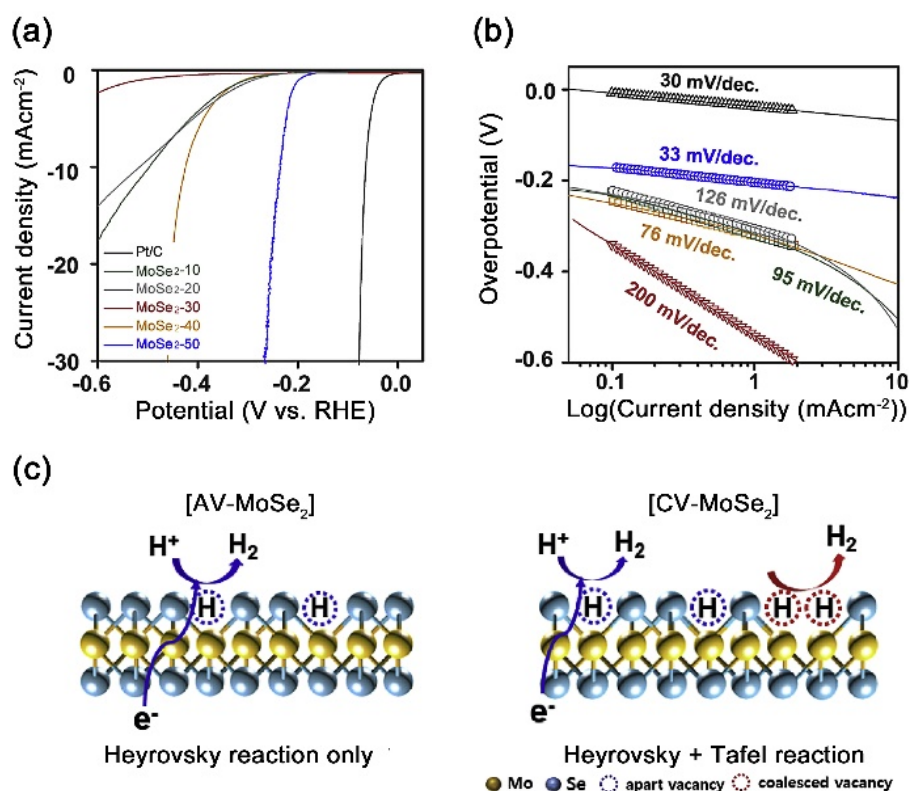


Figure 2. (a) HER polarization curve and (b) corresponding Tafel slopes of MoSe₂-10, 20, 30, 40, 50 and Pt/C in 0.5 M H₂SO₄ aqueous solution. (c) Schematic explanation of HER in AV- and CV-MoSe₂, which exhibit process of Tafel reaction in the coalesced Se-vacancy for hydrogen evolution. Reproduced and adapted from Ref. [79]; Copyright (2019), Elsevier.

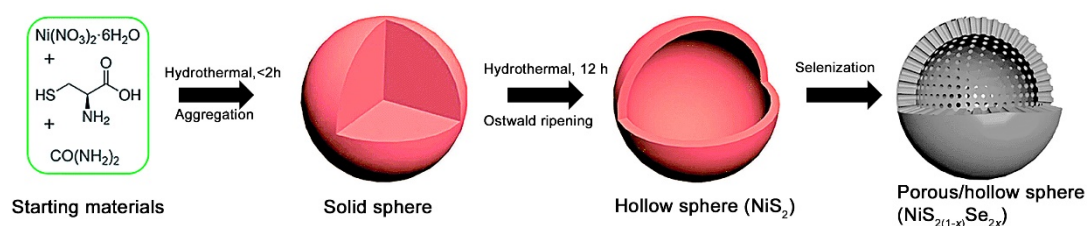
2.1.2. Hollow and Porous Structured Using NiS_{2(1-x)}Se_{2x} in Neutral Condition

In the recent past, neutral-pH overall water electrolysis has been considered the new efficient energy conversion alternative, as it can lower the cost of electrolysis devices without requiring costly membranes, and several electrolysis cells usually operate in neutral pH [95–97]. However, owing to low ionic concentrations and significant ohmic loss, electrocatalysts exhibiting excellent HER/OER performances in neutral pH are rare [98–101]. Only several Co- or Ni-based catalysts, such as CoP, Co₃S₄, and Ni₃Se₄, have been known to exhibit moderate performance under neutral media [102–105]. In addition, most of them exhibit less efficient catalytic performance than noble metals such as Pt- and Ru/Ir-based catalysts and generally suffer major long-term stability losses [104–106]. Under such situations, optimizing the relatively low-cost bifunctional electrocatalysts for water splitting with high performance and stability in neutral media is a crucial task, even though it entails great challenges. In recent years, TMDs have drawn considerable interest in terms of their ideal atomic structure, good electrochemical stability, and high electron transport, and many related studies on water splitting have been published [28,107–109]. Among them, MS_{2(1-x)}Se_{2x} compounds, referred to as metal (di)sulfoselenide, provide a fascinating promise, enabling accurate customizable electrocatalytic and other physiochemical characteristics. Zhuo et al. reported that ternary MS_{2(1-x)}Se_{2x} can accomplish a relatively low HER overpotential (69 mV at 10 mA cm⁻²) through customizable HER electrical properties under acidic conditions [110]. Similarly, improved catalytic efficiency was also reported for ternary Mo(Se_{0.85}S_{0.15})₂, WS_{2(1-x)}Se_{2x}, and Co(S_xSe_{1-x}) [111–114]. Although these indicated electrocatalysts can exhibit high HER/OER performances under acid or alkaline conditions, few of them show neutral-pH reactivity.

In this study, Ni-based catalysts, NiS_{2(1-x)}Se_{2x}, were fabricated and investigated to confirm HER/OER activities owing to their advantages such as eco-friendly features and low cost of Ni.

Further, Ni dichalcogenides have exhibited relatively high activities for either HER or OER under neutral-pH conditions [97,115]. Furthermore, to obtain a large number of catalytic active sites and decrease diffusion of charge and mass transport, one common strategy is to model and develop porous/hollow micro/nanostructured catalysts [48,49]. With these discussions, ternary nickel sulfoselenides ($\text{NiS}_{2(1-x)}\text{Se}_{2x}$) porous/hollow spheres were synthesized via a facile hydrothermal using the L-cysteine and selenization method.

Scheme 8 depicts the fabrication process for the ternary $\text{NiS}_{2(1-x)}\text{Se}_{2x}$ porous/hollow spheres. $\text{Ni}(\text{NO}_3)_2 \cdot 6\text{H}_2\text{O}$, urea, and L-cysteine were used to synthesize the NiS_2 hollow spheres precursor via heating at 140°C for 12 h, and the as-synthesized precursors were dried in a vacuum oven at 60°C for 6 h. Thereafter, for selenization, three different mass ratios of NiS_2 and Se powder were used (1:2, 1:5, and 1:10), which were heated to 450°C in a furnace for 2–5 h.



Scheme 8. Schematic diagram for synthesis of ternary $\text{NiS}_{2(1-x)}\text{Se}_{2x}$ porous/hollow structure via NiS_2 . Reproduced and adapted from Ref. [116]; Copyright (2019), The Royal Society of Chemistry.

Figure 3a exhibits the morphological aspects of the as-prepared NiS_2 precursor by transmission electron microscopy (TEM), minimizing the interfacial energy of hollow spheres based on the Ostwald ripening process. Subsequently, $\text{NiS}_{2(1-x)}\text{Se}_{2x}$ porous/hollow spheres were synthesized by thermal selenization using the NiS_2 precursor and Se powder in Ar gas. In this process, the Se/S atomic ratio was adjusted by varying the amount of Se powder and the reaction time (Figure 3b). Figure 3c, exhibiting the high-resolution TEM (HRTEM) image and the corresponding line scan outlined in a white rectangle, indicates the well-matched lattice fringes of the (200) plane with a lattice distance of 0.291 nm, slightly larger than that of standard NiS_2 (0.284 nm). The HAADF image and the corresponding EDX mapping of $\text{Ni}(\text{S}_{0.5}\text{Se}_{0.5})_2$ demonstrate the presence and homogeneous distribution of Ni, S, and Se element around the whole hollow structure (Figure 3d).

The powder X-ray diffraction (PXRD) patterns exhibit the NiS_2 hollow spheres before and after the thermal selenization process of a Pa3, corresponding to JCPDS no. 88-1709 (Figure 4a). However, the diffraction peaks of $\text{Ni}(\text{S}_{0.5}\text{Se}_{0.5})_2$ shift to a small angle compared to those of pure NiS_2 because of the larger atomic sizes of Se than S (inset of Figure 4a). The ternary $\text{NiS}_{2(1-x)}\text{Se}_{2x}$ compound is shown to have combined effects. Atoms of the transition metal Ni are offered as superior water splitting sites and have a strong electrostatic affinity with the hydroxide group in neutral media owing to plenty of unfilled *d* orbitals. In addition, the morphology modified by selenization offers a rough surface area, and the highly porous structure not only provides additional exposed catalytically active sites but also facilitates more active species to access the active sites. In addition, intrinsic catalytic activity can be improved by generating electrolytic diffusion/penetration and mass/electron diffusion systems more effectively. The results have been indicated using the N_2 sorption isotherm (Figure 4b). The unusual hierarchical hollow spheres were found to have a wide Brunauer-Emmett-Teller (BET) surface area of $91\text{ m}^2\text{ g}^{-1}$ with a pore diameter distribution primarily within the range 4–10 nm. Furthermore, anion doping efficiently modifies the electronic Ni structure, which is helpful in maximizing the adsorption free energy of process intermediates and improving the catalytic ability intrinsic to them. Therefore, this ternary $\text{NiS}_{2(1-x)}\text{Se}_{2x}$ material was considered to be a highly efficient and stable electrocatalyst for overall water splitting in neutral media.

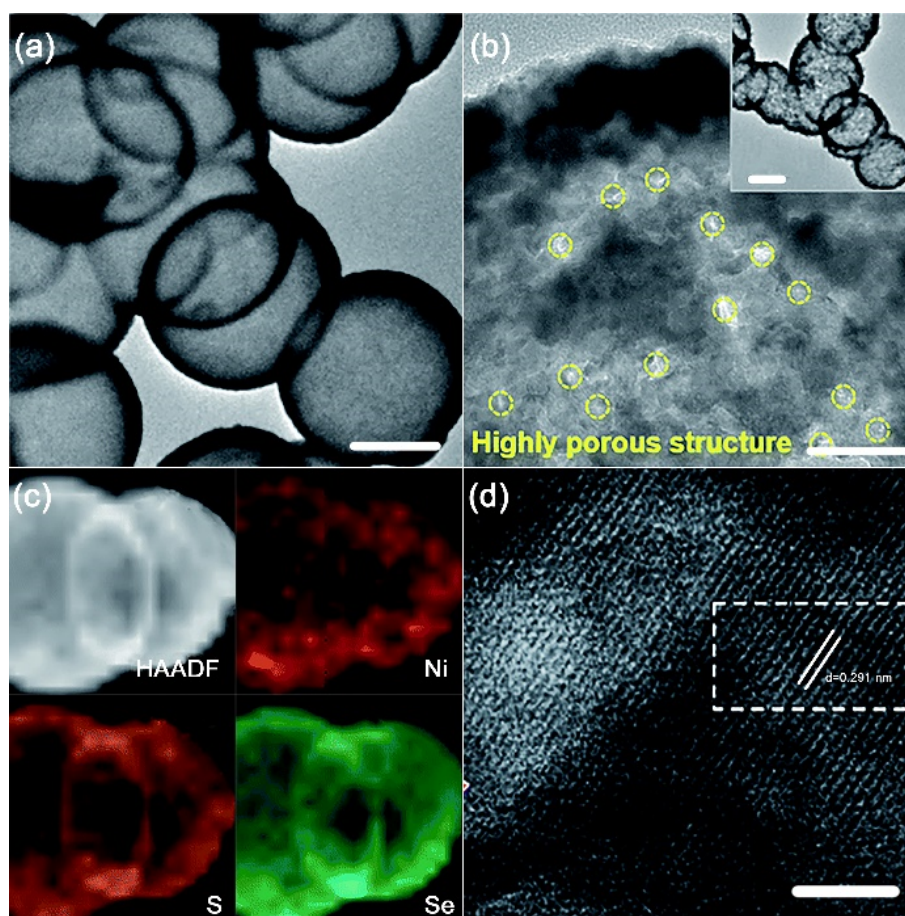


Figure 3. Transmission electron microscopy (TEM) image of (a) NiS_2 precursor and (b) $\text{NiS}_{2(1-x)}\text{Se}_{2x}$. The inset in (b) displays the surface of $\text{NiS}_{2(1-x)}\text{Se}_{2x}$. (c) Elemental mapping images of $\text{NiS}_{2(1-x)}\text{Se}_{2x}$, and (d) high-resolution TEM image of $\text{NiS}_{2(1-x)}\text{Se}_{2x}$. The bars indicate (a) 0.5 μm , (b) 50 nm, and (d) 5 nm. Reproduced and adapted from Ref. [116]; Copyright (2019), The Royal Society of Chemistry.

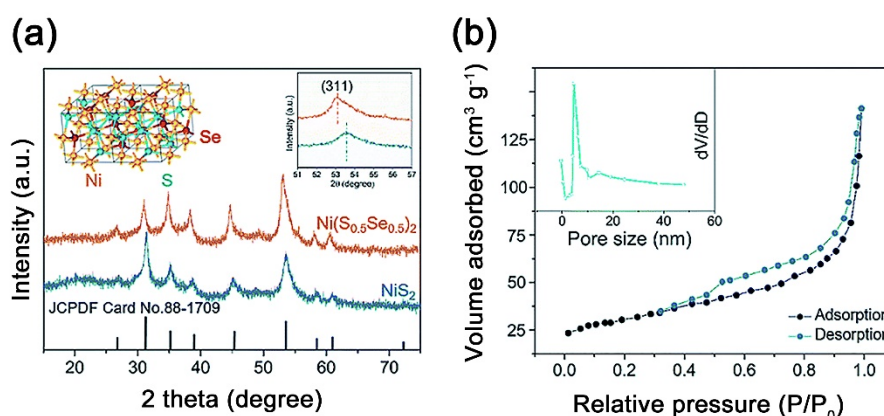


Figure 4. (a) X-ray diffraction (XRD) pattern of $\text{NiS}_{2(1-x)}\text{Se}_{2x}$ (red line) and NiS_2 (blue line). The inset of (a) is crystal structure. (b) N_2 sorption isotherm and measured pore size (the inset of (b)) of $\text{NiS}_{2(1-x)}\text{Se}_{2x}$. Reproduced and adapted from Ref. [116]; Copyright (2019), The Royal Society of Chemistry.

Figure 5a indicates that, among the samples, $\text{Ni}(\text{S}_{0.5}\text{Se}_{0.5})_2$ has the highest HER activity. It also displays the lowest Tafel slope (Figure 5b). The lowest charge transfer resistance was demonstrated by electrochemical impedance spectroscopy, performed to investigate more detailed electron-transfer kinetics (Figure 5c). Under neutral conditions, the HER pathway may be identical to that in alkaline conditions via the Volmer–Heyrovsky cycle. As indicated by the abovementioned results, the Ni

atom has a strong electrostatic affinity with the hydroxide group for water dissociation ability to produce H atoms for the primary Volmer step. However, in Heyrovsky's process, the free energy of H adsorption, when H atoms on the layer of catalysts are formed into H_2 , is such that the disulfided Ni site is too strong, whereas the diselenided Ni site is too weak. Therefore, by changing the Se/S ratio, the free energy of H adsorption, which can increase the HER operation, is optimized. In the chronoamperometry (CA) performed to demonstrate long-term durability, a significant property in electrocatalysts, it remained without degradation for 20 h, and the HER performance was mostly unchanged after 2000 continuous cyclic voltammetry (CV) cycles (Figure 5d).

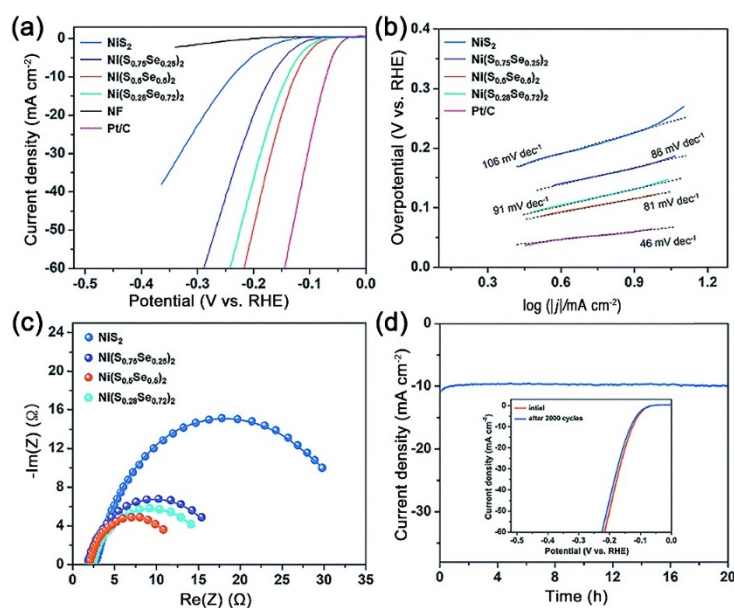


Figure 5. HER electrocatalytic performance in neutral condition. (a) Polarization curves and (b) the corresponding Tafel plots for the catalysts. (c) Nyquist plots scanned at -0.25 V (vs. RHE) and (d) time-dependent current density curve of the $Ni(S_{0.5}Se_{0.5})_2$ at overpotential 125 mV. The inset exhibits linear sweep voltammetry (LSV) curves before and after 2000 cyclic voltammetry (CV) cycles to confirm stability. Reproduced and adapted from Ref. [116]; Copyright (2019), The Royal Society of Chemistry.

The electrocatalytic oxygen generation was performed under the same conditions (Figure 6a). Similarly, the polarization curve had an overpotential of 501 mV to reach the current density of 10 mA cm^{-2} of $Ni(S_{0.5}Se_{0.5})_2$ among samples, compared to the standard IrO_2 catalyst, and the lowest Tafel slope of 94 mV dec^{-1} (Figure 6b). This resulted in a desirable electronic configuration and specific active sites for adsorption through the anion-doping activity of oxygen-rich groups. Similar to previously reported mechanisms for other metal chalcogenide electrocatalysts, the Ni cation exists as an actual active species with the oxide species (NiO_x) on the surface of the OER catalyst and forms the shell/core $NiO_x/Ni(S_{0.5}Se_{0.5})_2$. Similar to the tendency of HER, the $Ni(S_{0.5}Se_{0.5})_2$ electrode with the smallest Tafel slope indicates the lowest resistance for charge transfer (Figure 6c). Performing CA to demonstrate long-term durability, $Ni(S_{0.5}Se_{0.5})_2$ electrode demonstrated good durability at a constant applied voltage value of 1.73 V without degradation for 20 h (Figure 6d). The OER performance was almost unchanged after 2000 continuous CV cycles (inset of Figure 6d).

Based on the above mentioned results, the ternary $NiS_{2(1-x)}Se_{2x}$ electrocatalysts were superior to other catalysts in terms of electrocatalytic efficiency under neutral conditions. $Ni(S_{0.5}Se_{0.5})_2$ hollow/porous spheres were used for both the cathode and the anode to perform the overall water splitting. As depicted in Figure 7a, the $Ni(S_{0.5}Se_{0.5})_2||Ni(S_{0.5}Se_{0.5})_2$ electrode requires 1.87 V at a current density of 10 mA cm^{-2} , whereas a typical $Pt/C||IrO_2$ couple electrode requires 1.94 V at the same current density. In comparison, the Ni-assembled electrolyzer could sustain current density at a steady voltage of 1.87 V for 12 h under neutral conditions, in contrast to the rapid decline in current density

for the Pt/C||IrO₂ couple-catalyzed cell under CA (Figure 7b). These results demonstrated that the latest method involving bifunctional electrocatalyst under neutral conditions is a successful practical application for the complete splitting of water.

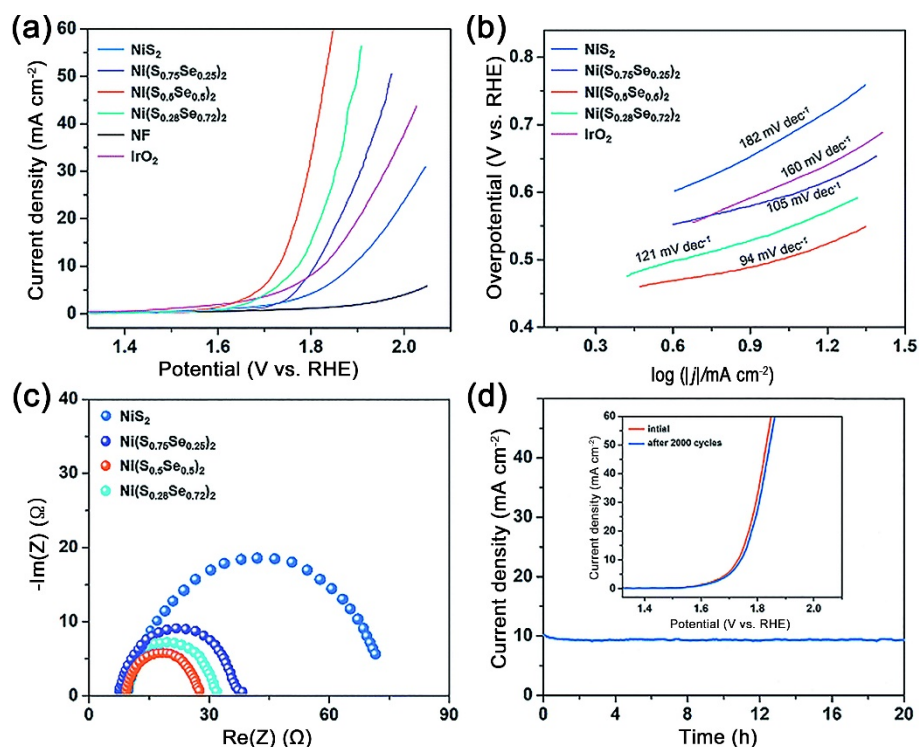


Figure 6. OER electrocatalytic performance in neutral condition. (a) Polarization curves and (b) the corresponding Tafel plots for the catalysts. (c) Nyquist plots scanned at 1.75 V (vs. RHE) and (d) time-dependent current density curve of the Ni(S_{0.5}Se_{0.5})₂ at 1.73 V. The inset exhibits LSV curves before and after 2000 CV cycles to confirm stability. Reproduced and adapted from Ref. [116]; Copyright (2019), The Royal Society of Chemistry.

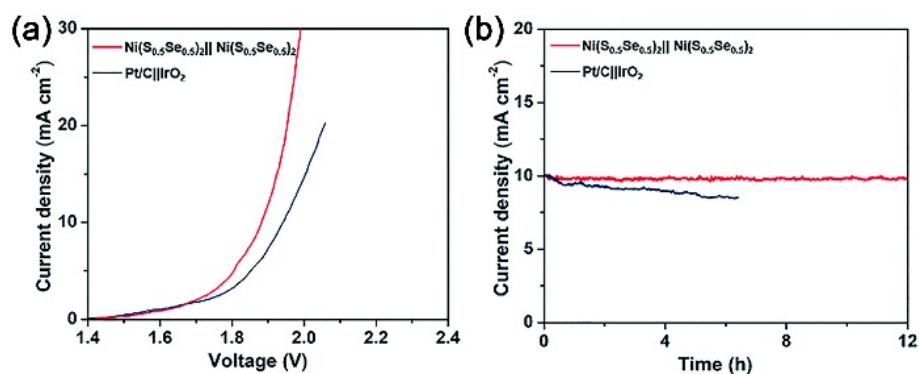
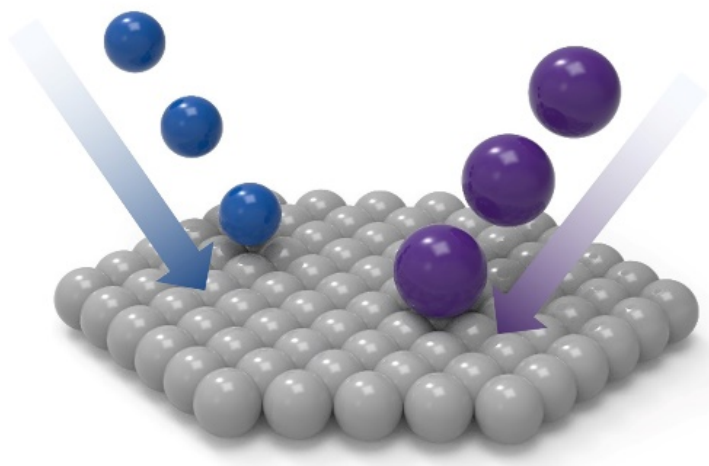


Figure 7. Overall water splitting in neutral condition. (a) Polarization curves for an Ni(S_{0.5}Se_{0.5})₂||Ni(S_{0.5}Se_{0.5})₂ and Pt/C||IrO₂ and (b) long-term durability test to achieve 10 mA cm⁻². Reproduced and adapted from Ref. [116]; Copyright (2019), The Royal Society of Chemistry.

2.2. Doping of Heteroatoms

Doping of heteroatoms, such as N, O, S, and P, is effective for increasing electrocatalyst activity by optimizing the electronic structure, increasing the number of active sites, and optimizing the intermediate formation regime (Scheme 9). Also, heteroatom doping can give graphene a variety of new or improved electromagnetic, physicochemical, optical, and structural properties. This greatly increases the arsenal of graphene materials and their potential for a wide range of applications. For

example, Lee et al. reported that MoP dual-doped with S and N exhibited a current density of 10 mA cm^{-2} for HER at an overpotential of 104 mV in 0.5 M H_2SO_4 [117]. Zang et al. recorded excellent catalytic efficiency for the HER with an overpotential of just 89 mV to give 10 mA cm^{-2} in 0.5 M H_2SO_4 for the Cu_3P NPs coated by an N, P-codoped carbon layer [118]. Furthermore, they reported that MOF-derived N, S, O-C@Co/ Co_9S_8 NPs acted as a multifunctional catalyst producing a current density of 10 mA cm^{-2} at 216 and 373 mV for HER and OER, respectively, in 1 M KOH [119]. Du's group reported Ir-doped $\text{NiV}(\text{OH})_2$ for overall water splitting [120].



Scheme 9. Illustration of heteroatoms on the NPs.

2.2.1. Ir-O-V Group Effect

The overall splitting of water in Ni-based layered double hydroxides (LDHs) occurs at quite high applied voltages, usually greater than 1.55 V [121–123]. NiV LDH was the initiating material, and doped Ir to create Ir-O-V and Ir atoms helped dissociate water and adjust the V atom and bridge O adsorption energies. The resulting NiVIr LDH exhibited superior HER and OER performances at overpotentials of 41 and 203 mV, respectively, at 10 mA cm^{-2} . The new NiVIr LDH achieved a total water electrolysis current density of 10 mA cm^{-2} at an approximate voltage of 1.49 V (as both cathode and anode), far lower than that of the Pt/C-IR/C catalytic complexes (1.60 V at 10 mA cm^{-2}) and seemed to set a new value for the overall water electrolysis cycle.

Figure 8a,b indicates that OER and HER are supposed to occur on V and bridge O, respectively, in the NiV LDH material. As seen in Figure 8b, after one Ni atom had been substituted by Ir, a simple decrease in the charge intensity was determined on the bridge oxygen atom located between the atoms V and Ir. The excessive adsorption of the hydrogen intermediates on the NiV LDH bridge oxygen could be reduced. Doping with Ir, however, seems to enhance charge density on V atoms, thereafter, decreasing upon excess adsorption of OER intermediates. In short, the Ir dopant is supposed to improve both OER and HER performance in the NiVIr LDH simultaneously. Morphologically, all three materials were identical, consisting of vertically grown nanosheet arrays on nickel foam (NF), as illustrated by scanning electron microscopy (SEM) images (Figure 8c). XRD patterns (Figure 8d) indicate that the NiV LDH and NiVIr LDH materials had phase compositions similar to that of $\alpha\text{-Ni}(\text{OH})_2$, and no additional diffraction peaks are found, indicating that the structure of the three materials were in one phase [124–126]. The (003) and (006) peaks of NiVIr LDH (Figure 8d) were shifted to lower diffractions angles by $\sim 0.3^\circ$ relative to NiV LDH, which suggests that the insertion of large Ir ions into NiV LDH induced lattice expansion.

The HER and OER performances of the catalysts were analyzed with 1 M KOH in N_2 - and O_2 -saturated solutions, respectively. Two reactions were practiced in the three-electrode system—the counter-electrode of the HER is the graphite rod and that of the OER is the platinum electrode [127–129]. The LSVs of the OER presented in Figure 9a indicate that the Ir-doped LDH demonstrates a lower

overpotential of 203 mV to fulfill a current density of 10 mA cm^{-2} , which is better than those of the $\text{Ni}(\text{OH})_2$, NiV LDH, and commercial Ir/C. The Ir-doped LDH material indicated an excellent HER activity, which has been proven by a low overpotential of 41 mV at 10 mA cm^{-2} (Figure 9b). To compare, the overpotential of the Ir-free LDH depicted at 10 mA cm^{-2} was 148 mV. Table 1 indicates the effects of the OER and HER performance calculated by Du's group [120].

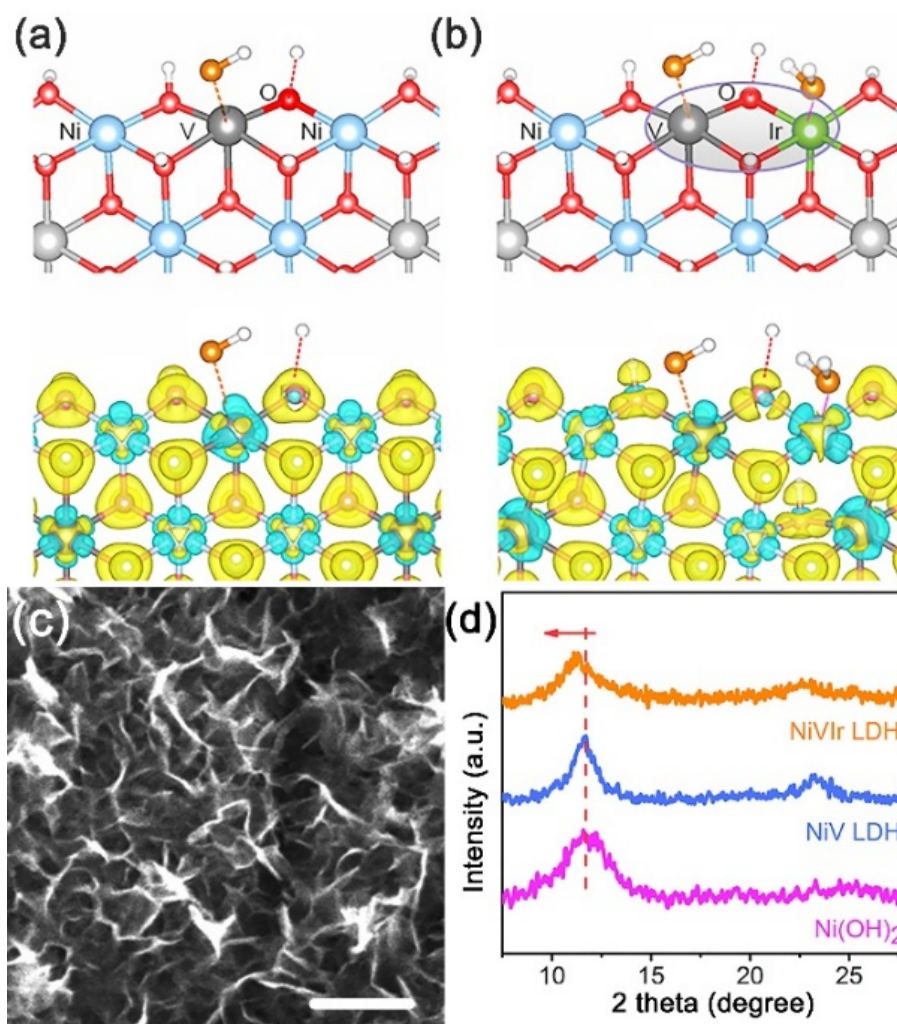


Figure 8. Active sites (top) in the overall water splitting process and differential-charge densities (down) of (a) NiV LDH and (b) NiVIr LDH. The isosurface value is 0.018 \AA^{-3} . (c) Scanning electron microscopy (SEM) image of surface morphology of NiVIr catalyst. (d) XRD spectrums of $\text{Ni}(\text{OH})_2$, NiV LDH, and NiVIr LDH, respectively. The bars indicate (c) 250 nm. Reproduced and adapted from Ref. [120]; Copyright (2019), American Chemical Society.

Du's group developed a new bifunctional catalyst comprising surface Ir-O-V catalytic groups, which were very effective for overall water electrolysis. The NiVIr LDH displays good catalytic attributes with an OER overpotential of 203 mV and an HER overpotential 41 mV at 10 mA cm^{-2} . The NiVIr LDH required 1.493 V at 10 mA cm^{-2} , performing better than the noble metallic Pt/C-Ir/C complex. More precisely, Ir, O, and V atoms of NiVIr LDH change the adsorption energy and electronic structure of the reaction course to acceptable values, which remarkably decrease the OER and HER overpotentials. Du's experiment demonstrates that doping with noble metals is an efficient way for improving the catalytic role of LDHs, which improves their ability and decreases expensive metal consumption.

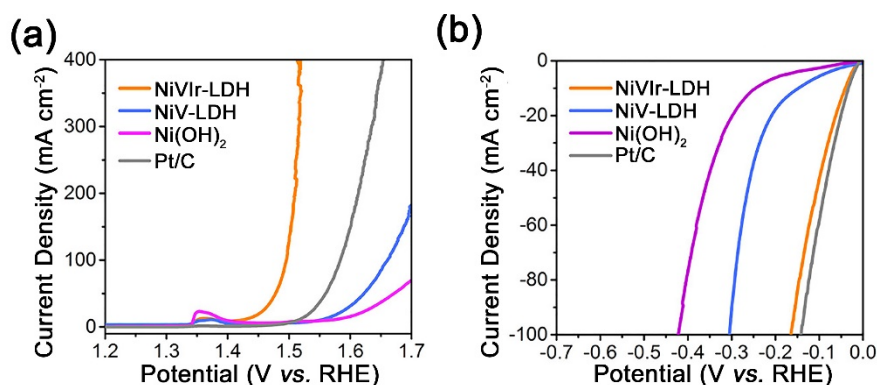


Figure 9. Polarization curves of (a) OER activity and (b) HER activity, respectively. Reproduced and adapted from Ref. [120]; Copyright (2019), American Chemical Society.

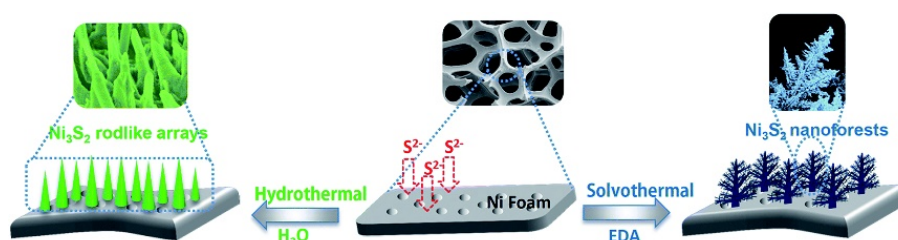
Table 1. Catalytic performance in OER and HER activity [120].

		NiVIr-LDH	NiV-LDH	Ni(OH) ₂	Ir/C	Pt/C
OER	Overpotential (mV)	203	319	337	284	-
	Tafel slope (mA dec ⁻¹)	55.3	119.2	214.1	86.8	-
HER	Overpotential (mV)	41	148	-	-	-
	Tafel slope (mA dec ⁻¹)	35.9	119.2	-	-	32.8

Both OER and HER activity for overpotential are performed at 10 mA cm⁻².

2.2.2. Effect of Multiplane Ni₃S₂ Superstructures

Liu's group suggested a new simple method for the synthesis of 3D Ni₃S₂ superstructures grown in situ on NFs using a one-step method of chemical etching (Scheme 10). Only the controlling solvent of the reaction allows the superstructures to be transformed into both nanoforest patterns and rod-like arrays. The technique is facile, economical, low-temperature, and has good commercial application prospects. Scheme 10 illustrates Ni₃S₂ superstructures formed on NF in disparate solvents (DI water, EDA). Arranged from disparate solvents, the 3D superstructures of the two species can be derived from the diverse kinetics of crystallization in disparate solvents. Thus, the product superstructures could be handled by regulating the chemical etching elements.



Scheme 10. Design of synthesizing Ni₃S₂ superstructures on nickel foam (NF). Reproduced and adapted from Ref. [130]; Copyright (2018), The Royal Society of Chemistry.

The Ni₃S₂ nanoforest and nanorod superstructures were further investigated using TEM and an analysis of the SAED patterns (Figure 10a–d). Figure 10a depicts a diameter of 200 nm and a length of approximately 1.5 μm, which corresponds with the SEM images. The rod tip amplification image (Figure 10b) clearly indicates a lattice at a distance of 0.28 nm, which can be related with the (110) crystal plane of the Ni₃S₂. Similarly, each nanoforest image (Figure 10c,d) is checked, and the branched structure is surrounded by an ultrathin nanosheets layer, synthesizing 3D hierarchical nanostructures. Since the electroactive sites are abundant, these ultrathin nanosheets offer outstanding electrochemical catalytic efficiencies.

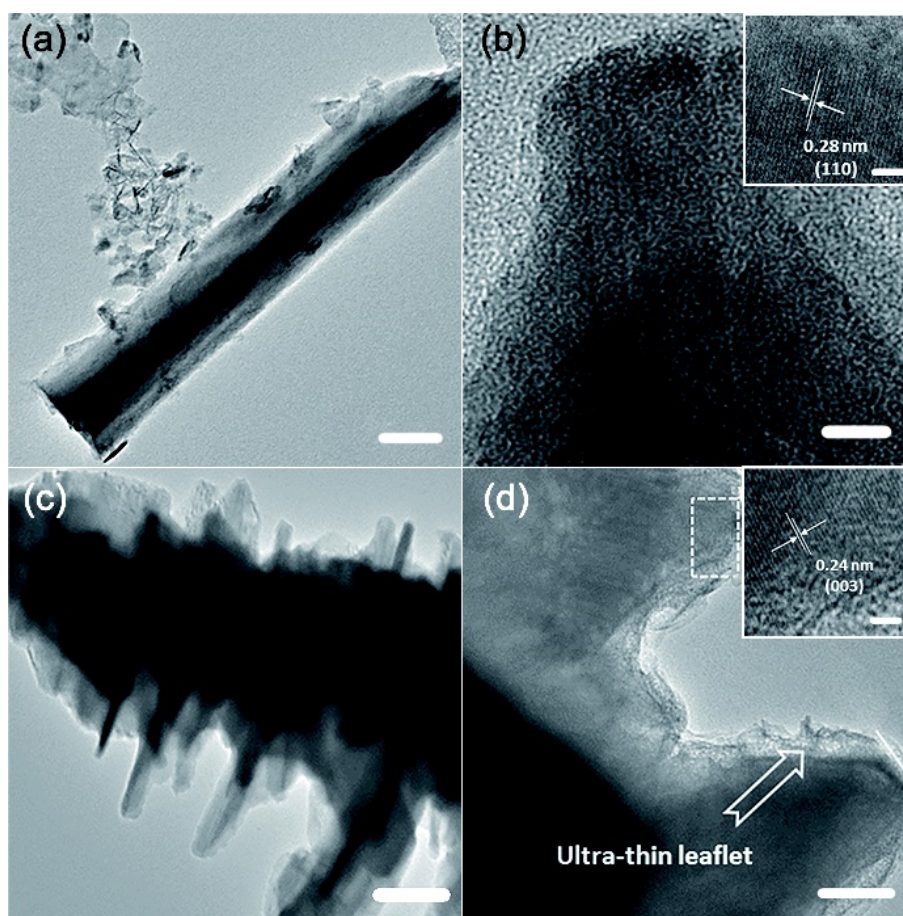


Figure 10. (a,b) TEM images of RA-Ni₃S₂/NF and (c,d) those of NA-Ni₃S₂/NF. The bars indicate 100 nm (a), 10 nm (b), 500 nm (c), and 100 nm (d). Reproduced and adapted from Ref. [130]; Copyright (2018), The Royal Society of Chemistry.

Ni₃S₂ was commonly used as water electrolysis catalysts because of its remarkable conductivity and activity [131–133]. To assess the electrocatalytic reactivity toward HER, tests were conducted on the synthesized 3D Ni₃S₂/NF superstructures in a 1.0 M KOH solution using a standard three-electrode system, in which the working electrode used the 2.0 cm² NF. The electrocatalytic reactivities of Pt/C on NF and bare NF were analyzed for comparison. Figure 11a displays their LSV curves. The synthesized superstructures of Ni₃S₂/NF display exceptional HER performance, in which the current densities are intensified at the used voltage. Rod-like array (RA)-Ni₃S₂/NF demands overpotentials of 0.146 and 0.255 V to provide current densities of 10 and 100 mA cm⁻², whereas NF-Ni₃S₂/NF demands those of 0.135 and 0.225 V. The NF-Ni₃S₂/NF has ultrathin leaflets, which decrease the overpotentials because leaflets provide more active sites for HER. Durability is also a significant criteria with respect to the electrocatalyst of the HER reaction. The long-period durability of the electrocatalysts was tested continuously in 1.0 M KOH over 5000 cycles (Figure 11b). Notably, both NF-Ni₃S₂/NF and RA-Ni₃S₂/NF exhibited a small loss of the current density of the cathode after 5000 CV cycles confirming the excellent durability. RA-Ni₃S₂/NF and NF-Ni₃S₂/NF were maintained at 15 and 20 mA cm⁻², respectively, when CA was measured for 50 h at a constant 150 mV vs. RHE (inset of Figure 11b).

Further research was carried out on the 3D Ni₃S₂ superstructures to assess the OER output in 1.0 M KOH. Figure 11c presents the LSV curves. All the 3D Ni₃S₂ superstructures demonstrated still higher efficiencies than bare NF. The 100-mA cm⁻² current densities of NF-Ni₃S₂/NF and RA-Ni₃S₂/NF exhibited 0.32 and 0.34 V overpotentials, respectively. Bare NF, in contrast, provided 100 mA cm⁻² at an overpotential of 0.51 V. Similar to the HER results, in OER, NF-Ni₃S₂/NF displayed a lower overpotential than RA-Ni₃S₂/NF. The Liu group found that NF-Ni₃S₂/NF could display better OER

performance relative to RA-Ni₃S₂/NF because of the abundance of particular surface areas of ultrathin nanosheets in NF-Ni₃S₂/NF, resulting in further active sites toward OER. Both NF-Ni₃S₂/NF and RA-Ni₃S₂/NF exhibited overpotentials of 0.23 and 0.27 V at 20 mA cm⁻², respectively, which displayed lower overpotential than other existing non-noble metal electrocatalysts [130,134–142]. To obtain the long-period durability of NF-Ni₃S₂/NF and RA-Ni₃S₂/NF toward OER, a long-period water oxidation was performed at 300 mV value of overpotential, and the OER reactions remained almost unchanged for 50 h (Figure 11d).

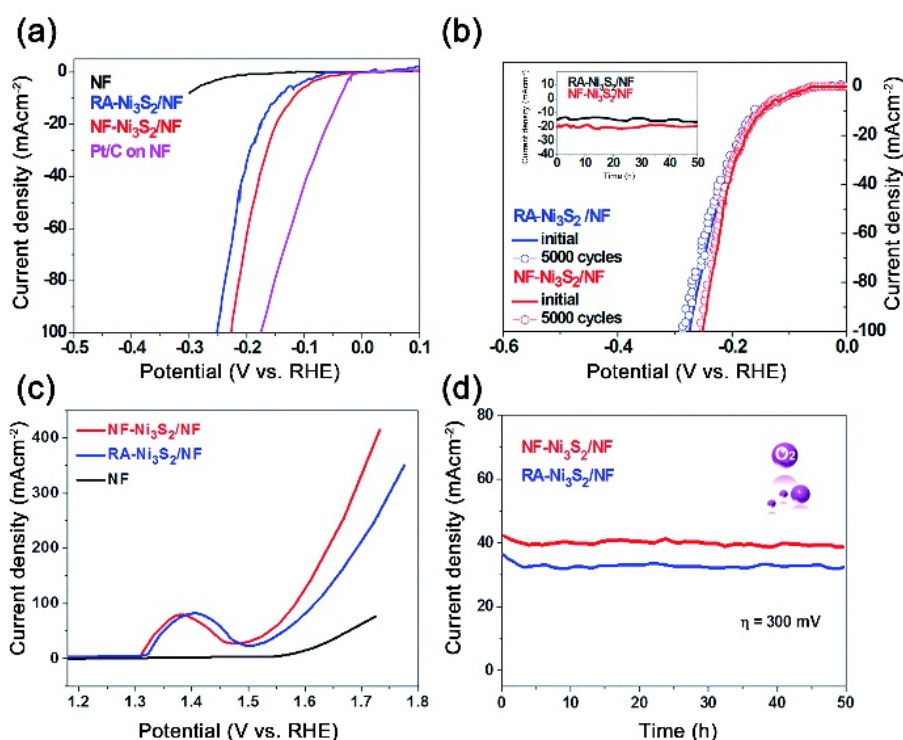


Figure 11. (a) HER polarization curves of bare NF, RA-Ni₃S₂/NF, NF-Ni₃S₂, Pt/C on NF. (b) Initial HER polarization curves and after 5000 cycles HER polarization curves of RA-Ni₃S₂/NF, NF-Ni₃S₂/NF in 1.0 M KOH. (c) OER polarization curves of bare NF, RA-Ni₃S₂/NF, NF-Ni₃S₂/NF in 1.0 M KOH. (d) Chronoamperometry of NF-Ni₃S₂/NF and RA-Ni₃S₂/NF for OER at 300 mV value of overpotential 1.0 M KOH. Reproduced and adapted from Ref. [130]; Copyright (2018), The Royal Society of Chemistry.

The Liu group further constructed an electrolyzer whose cathode and anode were both composed of the synthesized catalysts in a solution of 1.0 M KOH. NF-Ni₃S₂/NF and RA-Ni₃S₂/NF impressively produced current densities of 10 mA cm⁻² at 1.59 and 1.62 V and combined overpotentials of approximately 360 and 390 mV, respectively (Figure 12a). The 3D Ni₃S₂/NF performed better than the IrO₂/C-Pt/C commercial couple (1.68 V at 10 mA cm⁻²) and the newly reported overall water splitting electrocatalysts [125,141,143–148]. In addition, when the experiments were executed at 1.63 V, the electrolyzer supplied steady current densities (RA-Ni₃S₂/NF is approximately 20 mA cm⁻² and NF-Ni₃S₂/NF is approximately 30 mA cm⁻²) and maintained then for more than 50 h (Figure 12b).

The 3D Ni₃S₂ superstructures of nanorod arrays and nanoforest patterns were well grown in NF through a simple one-step method of chemical etching. The synthesized 3D Ni₃S₂ superstructures demonstrated considerable efficiency in HER, and the stability remained for more than 50 h. In addition, the 3D Ni₃S₂ superstructures consisted of a cathode and an anode for bifunctional water electrolysis with outstanding activity and notable long-time duration.

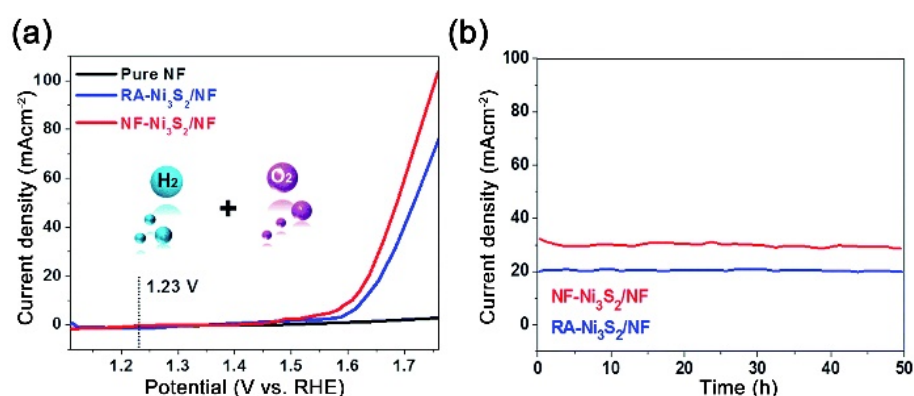
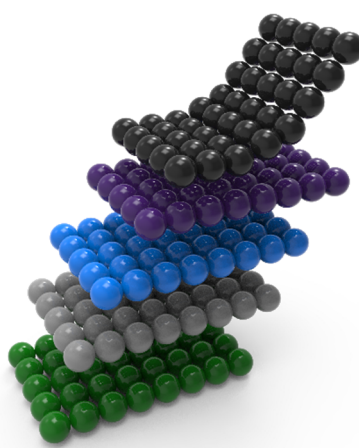


Figure 12. (a) OER polarization curves and (b) CA of RA-Ni₃S₂/NF, NF-Ni₃S₂/NF at 1.63 V in 1.0 M KOH. Reproduced and adapted from Ref. [130]; Copyright (2018), The Royal Society of Chemistry.

2.3. Heterostructure

The heterostructure idea originates from the physics of semiconductors (Scheme 11). In general, heterostructures can be characterized as hybrid structures consisting of interfaces formed using various solid-state materials, such as conductors, insulators, and semiconductors [70]. Heterostructures provide an ability to produce effective solar cells from highly absorbing thin-film materials without major losses by electron-hole recombination on the front side. Normally, heterostructures of 2D materials offer a way to study different phenomena and open up unprecedented possibilities to combine them for technological use. Such layers are very different from previous 3D semiconductor heterostructures, as each layer acts simultaneously as a bulk material and an interface, reducing the amount of load displacement within each layer. Nevertheless, the movement of charges between the layers may be very large, producing huge electrical fields and providing intriguing possibilities in the field of band-structure engineering. However, the key problem with hetero junctions is the lattice mismatch caused defect, which usually degrades the output of the system. It is normal for two different materials to have specific lattice parameters. If these components are put on top of each other.



Scheme 11. Illustration of various layers of heterostructure materials.

2.3.1. Components as the Ni-Based Heterostructure

In general, Ni-based composites are attractive catalysts in water splitting reactions because of the earth-abundance and low cost of Ni, and the components can affect their performance [149–156]. In addition, it has been revealed that Ni-based compounds can be used as catalysts for OER only by controlling counter-ion forms. The integration of the active OER (Ni₃N) and HER (NiMoN)

catalysts as heterostructures was stated by Fu's group through a well-designed path for efficient water splitting [156].

Figure 13 demonstrates the protocol for the synthesis of Ni₃N-NiMoN heterostructures. Ni-Mo-O nanosheets were synthesized on carbon cloth (CC) by hydrothermal reaction, and then the Ni₃N-NiMoN heterostructure was synthesized in the presence of ammonia gas by nitridation with Ni-Mo-O nanosheets. Bonding between Ni₃N and NiMoN can be easily formed owing to Ni-Mo-O precursor containing Ni and Mo.

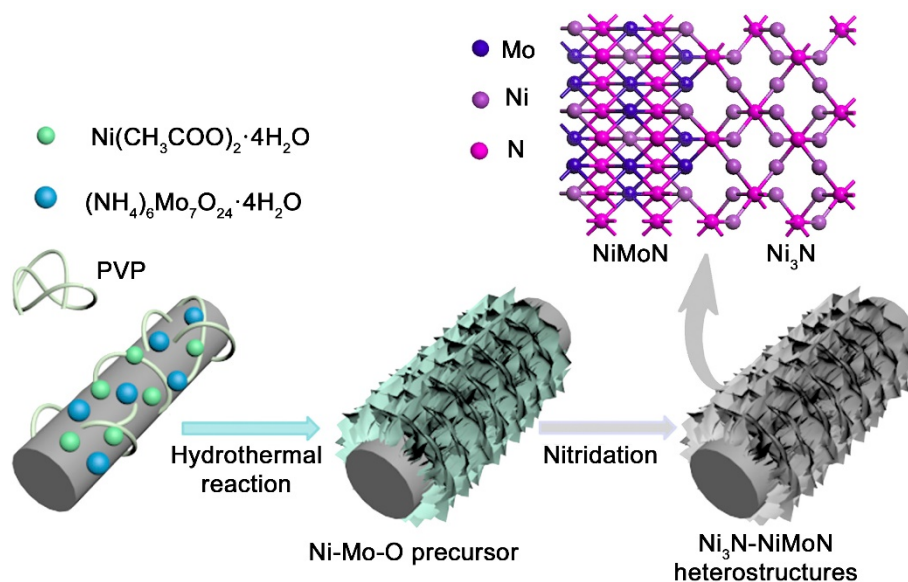


Figure 13. Illustration for the synthesis of Ni₃N-NiMoN heterostructure. Reproduced and adapted from Ref. [156]; Copyright (2018), Elsevier.

The Ni₃N-NiMoN nanosheet structures on CC are well maintained without any apparent collapse (Figure 14a,b). The lattice distances in the HRTEM images are 0.21 and 0.25 nm, which exhibit a good match with the (111) plane of Ni₃N and the (100) plane of Ni_{0.2}Mo_{0.8}N, respectively. We have already mentioned that presence of Ni₃N and NiMoN can make both the catalysts perform good OER and HER activity. The elemental mapping of Mo (yellow), Ni (cyan), and N (green) demonstrated uniform dispersion on the CC (Figure 14c–f) because Ni-N and Ni-Mo-N were successfully synthesized by controlling the reaction in the presence of ammonia gas.

One of the significant factors in the catalyst is long-term stability. A durability experiment is carried out in 5000 cycles using the Ni₃N-NiMoN-5 catalyst for 20 h (Figure 15b). The results indicate that the Ni₃N-NiMoN-5 catalyst exhibits excellent stability under alkaline conditions in a long-term electrochemical system (Ni₃N-NiMoN-5: 277 mV at 10 mA cm⁻², Ni₃N-NiMoN-4, Ni₃N-NiMoN-6, RuO₂, and NiMoO-1 are about 300 mV, 343 mV, 325 mV, and 356 mV at 10 mA cm⁻², respectively). These results of the excellent HER activity observed in an alkaline system imply that the catalyst can easily cooperate without most noble metals such as Ru, Pt, and Ir OER catalysts, which typically exhibit good behavior in alkaline media. Figure 15c presents the polarization curves without the iR-corrections. The Ni₃N-NiMoN-5 catalyst exhibits the high-performance OER output and needs a modest overpotential of 277 mV to reach the current densities of 10 mA cm⁻², whereas those for RuO₂ and NiMoO-1 are approximately 325 and 356 mV. Fu's group has already demonstrated Ni₃N-based materials to be active for OER in several earlier studies [152,153,157]. Therefore, earlier reports have suggested that Ni₃N is an effective catalyst for OER. Further, the long-term durability of Ni₃N-NiMoN-5 for OER was implemented based on its relevance for scientific basis (Figure 15d). The Ni₃N-NiMoN-5 catalyst's polarization curve exhibits a slight change in current density compared to

the original. In addition, the time–current density curve indicated that after 20 h of OER activity, the operation degrades only marginally.

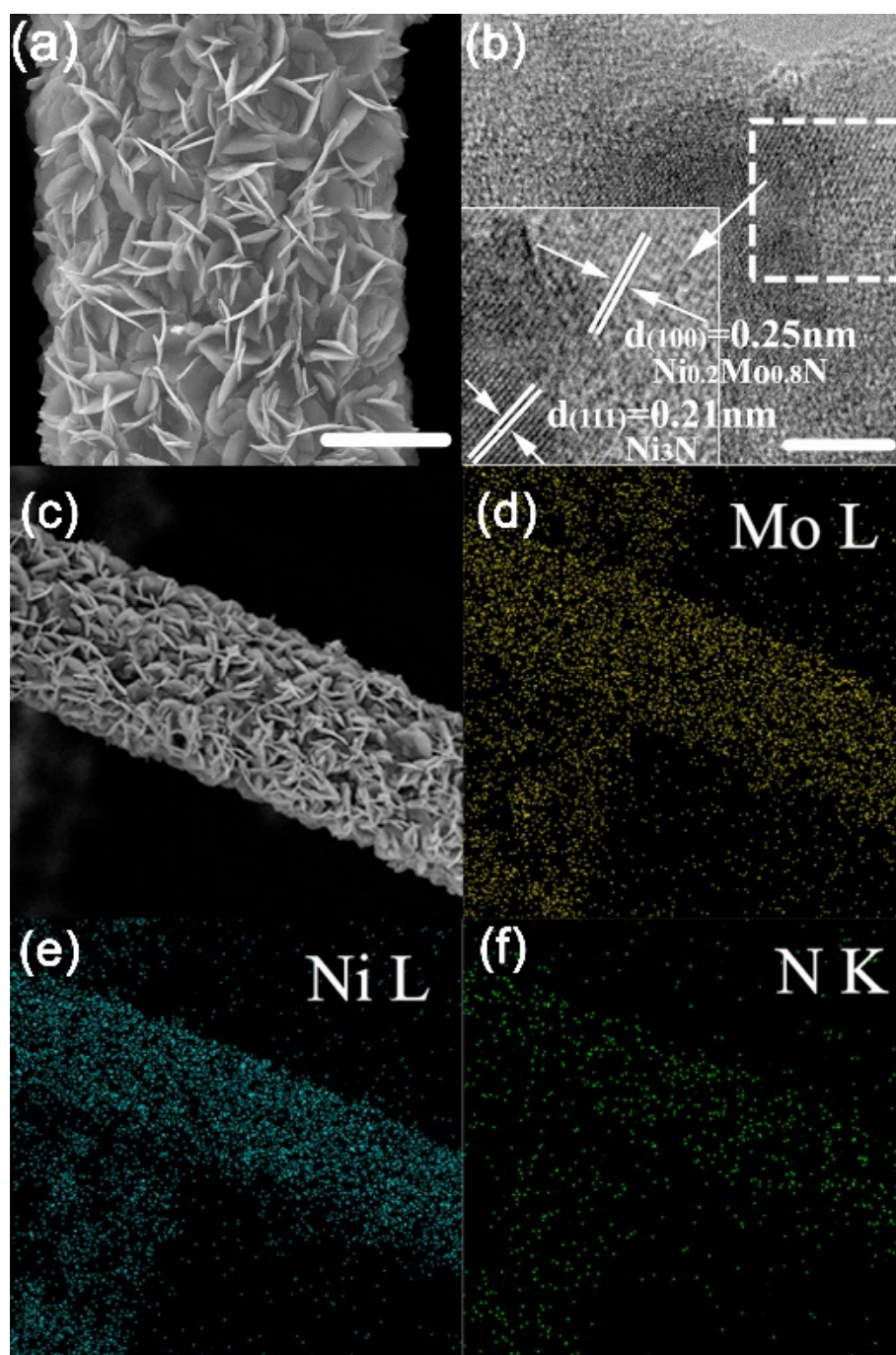


Figure 14. (a) SEM, (b) high-resolution TEM (HRTEM), (c) HAADF images of $\text{Ni}_3\text{N-NiMoN}$ heterostructure, (d–f) elemental mapping images of Mo, Ni, and N for $\text{Ni}_3\text{N-NiMoN}$ heterostructure, respectively. The bars indicate (a) 5 μm and (b) 5 nm. Reproduced and adapted from Ref. [156]; Copyright (2018), Elsevier.

In this study, $\text{Ni}_3\text{N-NiMoN}$ could be specifically applied to the anode (HER) and cathode (OER), as the overall water splitting catalysts demonstrate high performance under the same alkaline state.

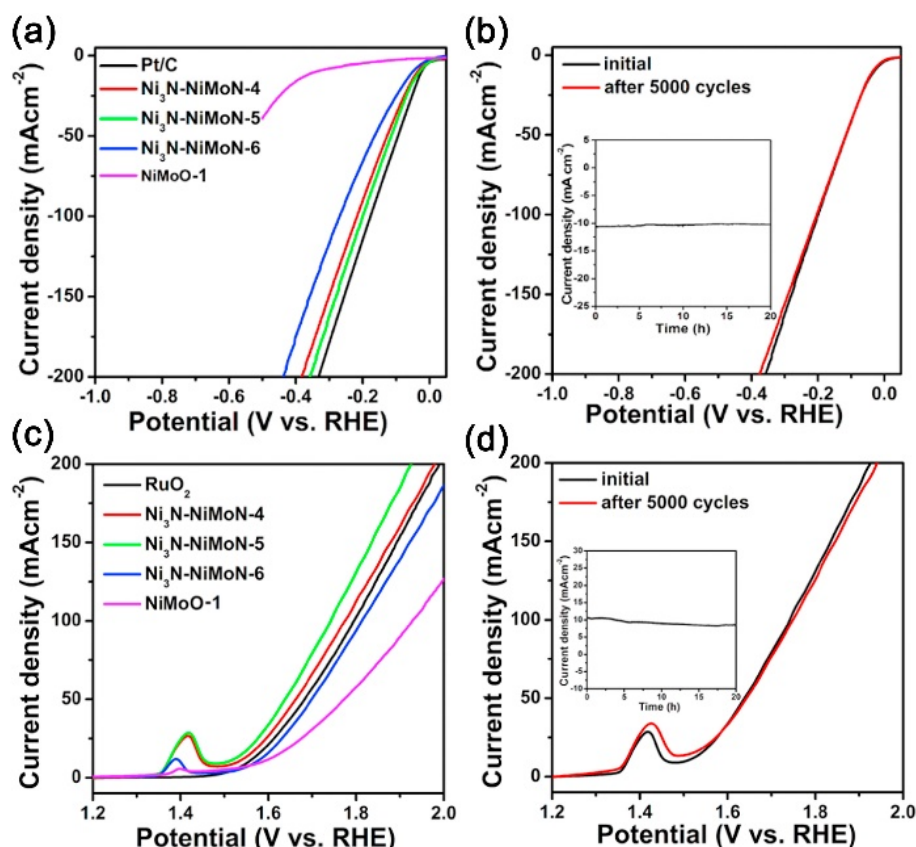


Figure 15. HER activity property of (a) polarization curves for Pt/C, various Ni₃N-NiMoN-X (X = 4, 5, 6; 400, 500, and 600 °C), (b) durability of Ni₃N-NiMoN-5 performed with a scan rate of 100 mV s⁻¹ initial and after 5 K cycles. Inset of (b) current depends on time curves. OER activity property of (c) polarization curves for RuO₂, various Ni₃N-NiMoN-X, and (d) durability of Ni₃N-NiMoN-5 performed with a scan rate of 100 mV s⁻¹ initial and after 5 K cycles. Inset of (d) current depends on time curves. Reproduced and adapted from Ref. [156]; Copyright (2018), Elsevier.

2.3.2. Co and β -Mo₂C NPs Composed of N-Doped CNTs

Recently, it has been reported that complexes of Co-based hybrid materials such as Co-N, Co-Pi, NiCo₂O₄, NiCo alloy, and others can improve catalytic performance in the OER [158–162]. Moreover, *M-C_x*, *M-S_x*, *M-P_x*, and *M-Se_x* (*M* = transition metal) exhibit optimal catalytic activity for HER [163–166]. In particular, molybdenum carbide (Mo₂C) exhibits brilliant HER activity in both alkaline and acidic systems because the electronic *d*-band model of molybdenum is similar to that of platinum [167–169]. Therefore, it has exhibited effective catalytic activity by combining the secondary phase/structure of Co and Mo-base as catalysts for the overall splitting of water in Ref. [170].

Melamine, which is commonly used as a precursor of nitrogen and carbon, has been used in this study. It was synthesized by mixing Mo and Co salt with facile heat treatment (Figure 16a). Figure 16b,c exhibits the tubular shape of Co/ β -Mo₂C@CNTs, in which nanotubes were encapsulated with Mo₂C and Co. The HRTEM image indicates that the lattice distance of 0.23 and 0.20 nm corresponds to the plane (101) of β -Mo₂C NPs and the plane (111) of Co NPs, respectively.

In the XRD patterns of Co/ β -Mo₂C@N-CNTs, Co, and β -Mo₂C peaks were mainly observed at $2\theta = 34.3^\circ$, 37.7° , 51.9° , 61.5° , 69.1° , 72.4° , and 74.5° well-matched with β -Mo₂C (JCPDS No. 35-0787), and peaks at around $2\theta = 44.2^\circ$, 51.7° , and 75.8° well-matched with Co (JCPDS No. 15-0787), respectively (Figure 17).

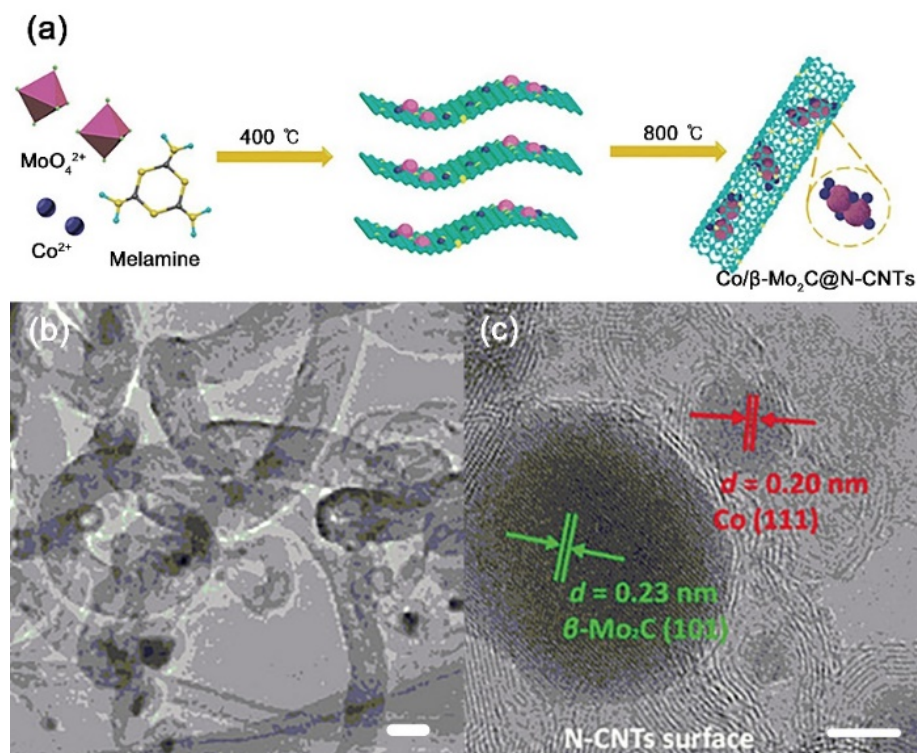


Figure 16. (a) Schematic image of synthesis Co/β-Mo₂C@N-CNTs, (b) TEM and (c) HRTEM image of Co/β-Mo₂C@N-CNTs. The bars indicate 20 nm (a) and 5 nm (b). Reproduced and adapted from Ref. [170]; Copyright (2019), Wiley.

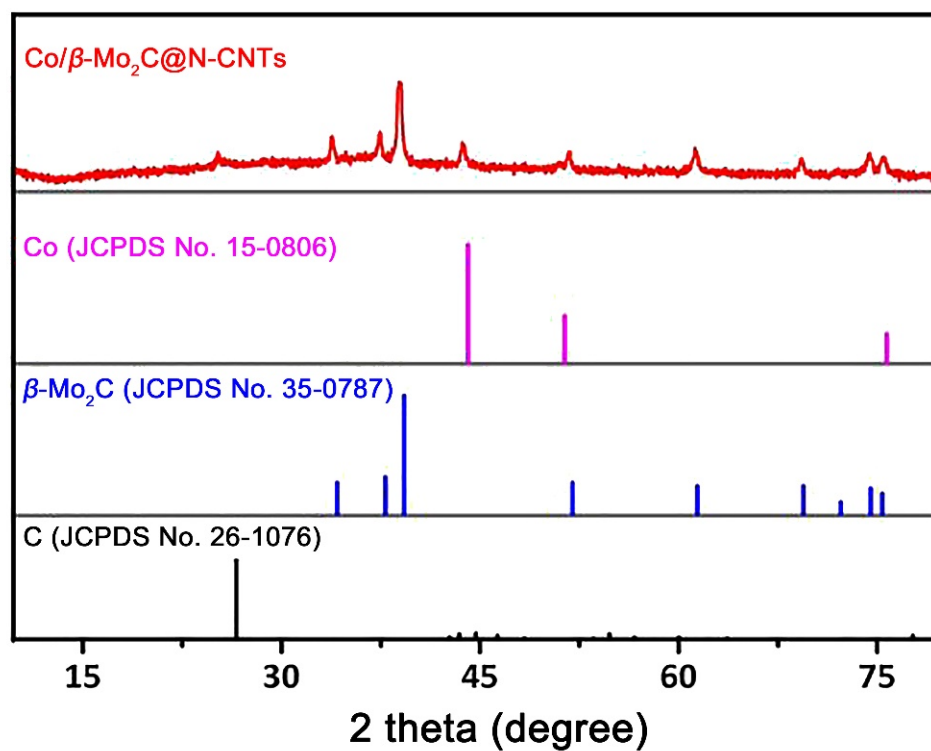


Figure 17. XRD of the Co/β-Mo₂C@N-CNTs, Co, and β-Mo₂C the well-defined peaks, respectively. Reproduced and adapted from Ref. [170]; Copyright (2019), Wiley.

Further, in this study, the efficiencies of HER and OER were measured using a standard three-electrode device. Table 2 presents the performance of each catalyst, such as overpotential,

Tafel plot, current density, and double-layer capacitance (C_{dl}). The performance of the three catalysts used in the HER activity was significantly inferior to that of Pt/C [170]. However, the heterostructure that used Co/ β -Mo₂C@N-CNTs as a catalyst displayed higher activity than others. The Co/ β -Mo₂C@N-CNTs still exhibited the highest current density when the geometric current density was further normalized to the corresponding C_{dl} value, thus suggesting that the hybrid is intrinsically most involved. Therefore, the HER performance of Co/ β -Mo₂C@N-CNTs compares favorably with the actions of many recorded Co- and Mo₂C-based representative electrocatalysts. These results indicate that the OER activity is impaired by Co doping. Moreover, the overpotential of IrO₂ as a reference catalyst was significantly higher than the Co/ β -Mo₂C@N-CNTs. Both OER and HER activity were tested in 1 M KOH.

Table 2. HER and OER activity in 1 M KOH electrolyte [170].

		Co/ β -Mo ₂ C@N-CNTs	Co@N-CNTs	Mo ₂ C@N-CNTs	Pt/C	IrO ₂
HER	η_{10} (mV)	170	275	452	36	-
	Tafel plot (mV dec ⁻¹)	92	115	171	-	-
	Current density (mA cm ⁻²)	0.14	0.020	0.053	-	-
	C_{dl} (mF cm ⁻²)	2.1	1.3	0.7	-	-
OER	η_{10} (mV)	356	-	-	-	377
	Tafel plot (mV dec ⁻¹)	67	90	188	-	-
	C_{dl} (mF cm ⁻²)	2.6	1.2	0.4	-	-

3. Redox-Mediated OER and ORR for LOBs with Soluble Redox Catalysts

3.1. Introduction

Although LOBs have attracted significant attention on account of high energy density, they still have certain limits such as uncertainty of electrolyte at high voltage, large overpotentials, and subsequent low cycling stability [72,73,171–175]. Researchers have focused on developing and modifying cathodes and electrocatalysts to promote the ORR and OER to address these problems. However, another problem—the deposition of byproducts such as Li₂O₂, Li₂CO₃, and LiOH on the catalysts—impedes the transfer of electrons, causing the overcrowding of electrolyte and oxygen mass transport [176–184]. As a solution of these issues, soluble redox catalysts, which enhance the ORR or OER and prevent deposition of byproducts to some degree, have been introduced recently [185–192]. In addition, Wang et al. have designed a new redox-flow lithium battery (RFLB) using redox mediators, which helps the current collector of the electrodes to be changed to separated energy storage tanks [193–196]. This idea has been successfully applied to address the abovementioned pressing problems with a non-aqueous LOB, resulting in a new device, the redox-flow LOB (RFLOB) [197]. Figure 18a presents the schematic of a couple of ORR and OER electrocatalysts and other components. In fact, the creation and decomposition of byproducts happen in the gas diffusion tank (GDT), spatially isolated from the cathode of the cell, which seamlessly eliminates pore-clogging problems and surface passivation. Furthermore, compared to the traditional enclosed battery, such a decoupled structure as an independent power source and energy storage gives an RFLOB great advantages such as optimization and versatility of operation of redox flow batteries [193–195]. In this study, tris{4-[2-(2-methoxyethoxy)ethoxy]phenyl}amine (TMPPA) and 2,5-di-*tert*-butyl-*p*-benzoquinone (DTBBQ) are used as OER and ORR catalysts, respectively, to address issues like corrosion, large overpotential owing to oxidation of Li₂O₂, and instability after long-term cycling (Figure 18b).

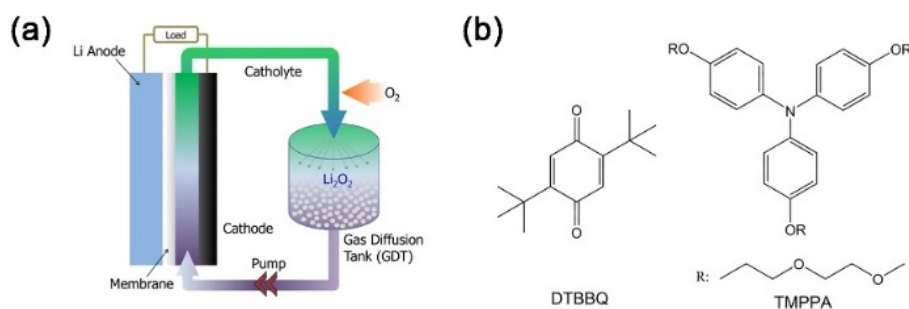


Figure 18. (a) Schematic diagram of the redox-flow lithium-oxygen batteries (RFLOB). (b) Molecular structure of the two redox mediator, 2,5-di-*tert*-butyl-*p*-benzoquinone (DTBBQ) and tris[4-(2-methoxyethoxy)ethoxy]phenyl)amine (TMPPA). Reproduced and adapted from Ref. [198]; Copyright (2016), American Chemical Society.

3.2. Application of TMPPA and DTBBQ as Redox Mediators to RFLOB

CV analyses were implemented to confirm the redox peak of TMPPA and DTBBQ (Figure 19a). The reversible redox peaks of DTBBQ and TMPPA are depicted at approximately 2.63 and 3.63 V (vs. Li/Li⁺), respectively, crossing the Li₂O₂ equilibrium potential at 2.96 V (vs. Li/Li⁺). Thermodynamically, this indicates that DTBBQ^{•−} may be reduced to O₂ and act as an ORR mediator that enhances Li₂O₂ production during the discharge step, whereas TMPPA^{•+} oxidizes Li₂O₂ and works as an OER transmitter substance that promotes Li₂O₂ decomposition during the charge step. A schematic displaying the redox-targeting reactions of TMPPA and DTBBQ with Li₂O₂ (Figure 19b) demonstrates the working mechanism of the RFLOB. The discharging potential of the RFLOB is determined by the discharging process, which includes the process through which the reduction of molecules in the catholyte flows into the cathodic section in the cell. After the catholyte flows back to the GDT, the generated DTBBQ^{•−} reduces O₂, where the gas is supplied, and produces Li₂O₂. The reaction of DTBBQ^{•−} with the oxygen molecules in this procedure includes only charge transfer at the tank's interface between the liquid and gas. The two reactions of discharging process are expressed as follows:

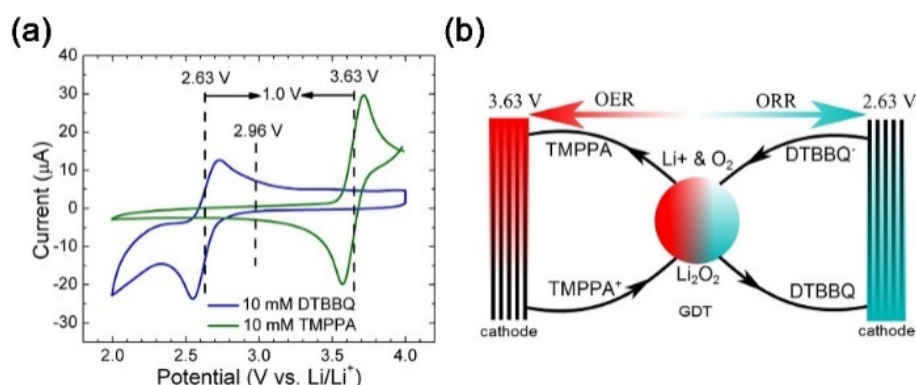
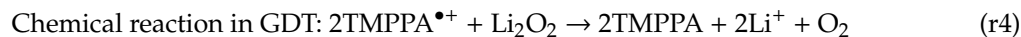


Figure 19. (a) CV of 10 mM DTBBQ (blue line) and TMPPA (green line) in TEGDME (1 M LiTFSI) electrolyte. (b) Illustration of demonstrating reactions DTBBQ^{•−}- and TMPPA-catalyzed ORR and OER during the charge and discharge processes of RFLOB. Reproduced and adapted from Ref. [198]; Copyright (2016), American Chemical Society.

Similarly, the charging potential of the cell is determined by the charging process, which implies the oxidation process of both the molecules in the cell. Thereafter, the generated TMPPA^{•+} oxidizes

Li_2O_2 , producing O_2 back into the GDT when the catholyte circulates. The detailed reactions of the charging step are explained as follows:



Further, as the reaction between redox mediators cannot occur during the charge and discharge steps, the mediators maintain stability with each other.

The OER and ORR reactions of the TMPPA and DTBBQ were analyzed using rotating disc electrode spectrometry (Figure 20a,b, respectively). In the case of the OER performance of TMPPA, despite the presence of Li_2O_2 in the electrolyte, no current was observed in the OER potential range. However, a steady-stage current of at least 0.26 mA cm^{-2} emerged at a potential above 3.70 V vs. Li/Li^+ , equivalent to the TMPPA oxidation, after 2 mM TMPPA was transferred to the above-mentioned electrolyte. This current density is considerably higher than the value of TMPPA alone ($\sim 0.16 \text{ mA cm}^{-2}$), suggesting that the reaction of $\text{TMPPA}^{\bullet+}$ with Li_2O_2 contributes to the increased current. Furthermore, the reaction is resistant to an N_2 - and O_2 -saturated solution, suggesting that the TMPPA may be impervious to O_2 during the measurement process. As illustrated in Figure 20b, DTBBQ's ORR efficiency in an O_2 -saturated electrolyte is significantly greater than that in an N_2 -saturated electrolyte, with the assumption that $\text{DTBBQ}^{\bullet-}$ can effectively minimize oxygen molecules. This phenomenon is similar to the catalytic effect of TMPPA.

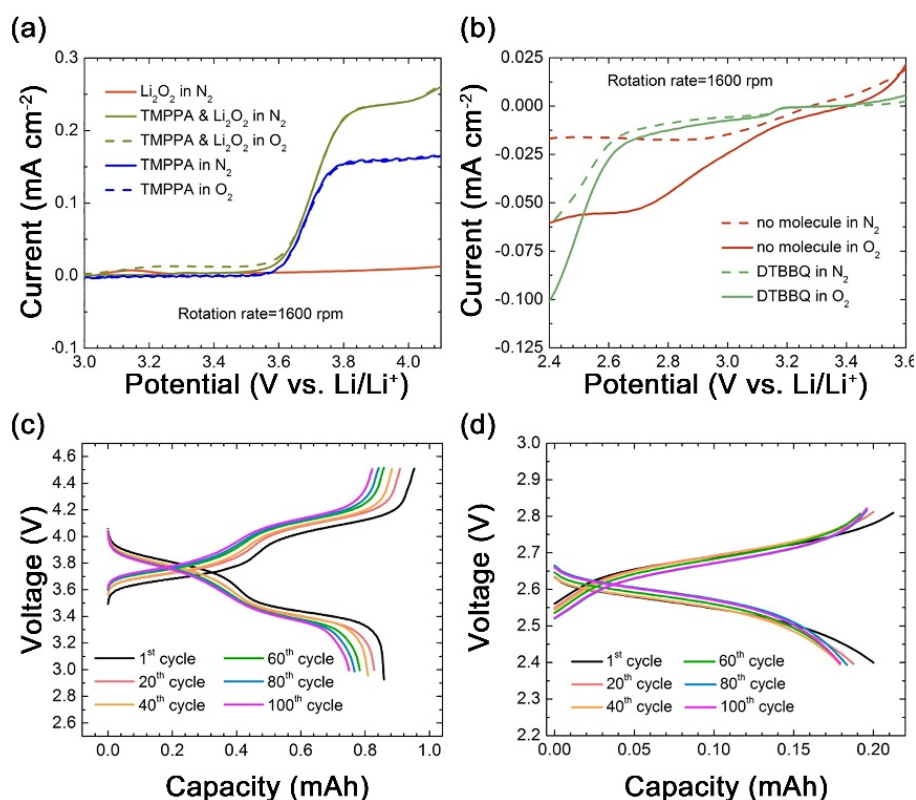


Figure 20. (a) RDE test of the OER reaction between 2 mM TMPPA and Li_2O_2 and (b) ORR reaction between 2 mM DTBBQ and O_2 gas in 0.10 M LiTFSI in TEGDME. Galvanostatic tests of (c) 20 mM TMPPA and (d) 20 mM DTBBQ analyzed in static lithium half-cells under an Ar atmosphere. Reproduced and adapted from Ref. [198]; Copyright (2016), American Chemical Society.

To scrutinize the stability of the redox mediators with long-term cycling, galvanostatic tests were conducted by employing TMPPA and DTBBQ as liquid cathodes in half-cells (Figure 20c,d,

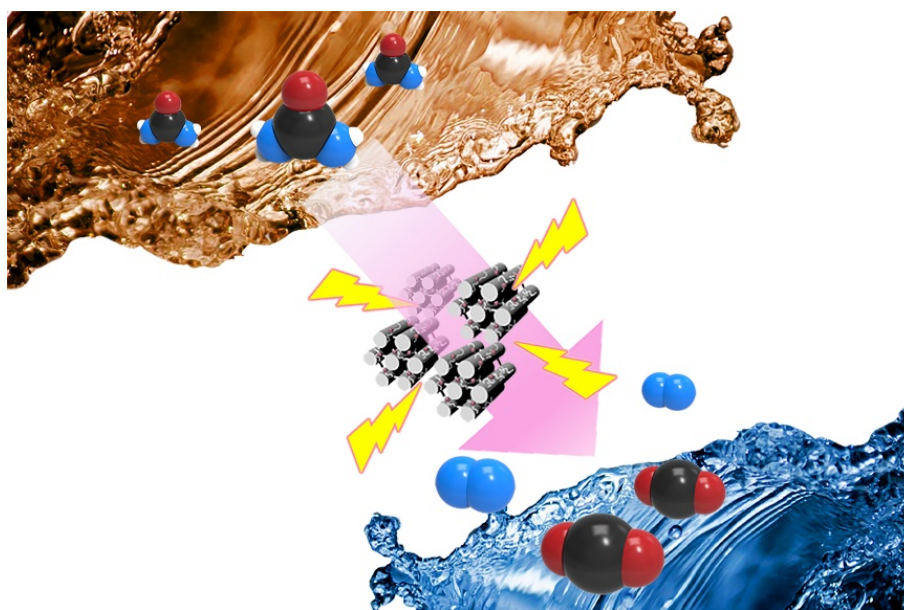
respectively). The two redox mediators exhibit outstanding electrochemical stabilities under Ar atmosphere. In particular, it is confirmed that the polymerization of molecules is effectively hindered and the development of the TMPPA radical cation and dication is also significantly stabilized because of the alkoxyl group on TMPPA's phenyl rings. The capacities of TMPPA and DTBBQ were maintained at 87.4% and 89.4%, respectively, after 100 cycles.

In this study, new redox catalysts TMPPA and DTBBQ have been introduced as a solution of pore-clogging issues and the passivation of the cathode surface. This novel device provides several benefits for large and high-density energy storage in terms of flexibility and scalability. However, TMPPA and DTBBQ need further improvement to be powerful enough for the RFLOB. For example, the degradation of mediators, particularly DTBBQ, after prolonged cycling induces a change in the voltage profiles, posing the main hurdle for pragmatic use. Moreover, the redox potentials of Li_2O_2 are slightly different from those of the redox mediators, which could cause overpotential losses during the discharge and charge processes. Therefore, additional research is needed to address the side reactions of the redox mediators in an O_2 atmosphere and the control redox potentials more accurately to alleviate voltage hysteresis.

4. Application of Hydrogen Production via HER and UOR Activities

4.1. Introduction

Among the numerous recently developed energy-saving electrolysis methods, urea electrolysis is extraordinarily interesting, allowing for the treatment of urea-rich sewage by reducing the urea in it to produce a clean, eco-friendly mass of H_2 energy [76,199]. In particular, the use of the UOR in ordinary water splitting potentially replaces the OER with a significant thermodynamic potential change from 1.23 V vs. RHE to a mere 0.37 V (Scheme 12). Urea is a suitable and promising storage medium for H_2 and CO_2 owing to it being highly dense, relatively nontoxic, inexpensive, robust, safe, and easy to carry and store. Nevertheless, the key problem is the existence of UOR, which experiences sluggish kinetics owing to a six-electron transfer cycle composed of gas evolution phases; thus, highly effective and inexpensive electrocatalysts are required to implement this outstanding model of energy conversion [200].



Scheme 12. Illustration of urea electrolysis by electrochemistry.

4.2. The Application of Electrocatalyst via Synthesis of Facile Melt-Infiltration

Figure 21 illustrates a simple Ni-Pd alloy NPs preparation strategy integrated into ordered mesoporous carbon (OMC) support with optimized nanostructures through necessary steps. First, Ni and Pd salts were melt-infiltrated on the OMC, and then Ni-Pd bimetallic salts were heat-treated under H₂ gas flow.

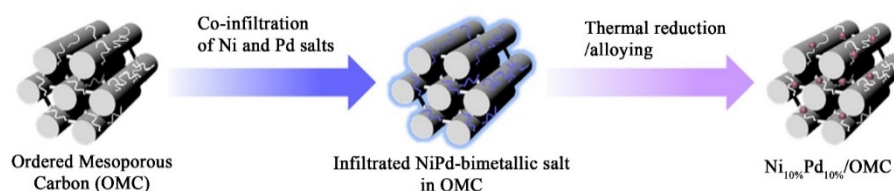


Figure 21. Schematic illustration for preparation of the bimetallic NiPd/OMC catalyst.

Consequently, the Ni-Pd salt is formed from the tiny Ni-Pd alloy NPs that are well dispersed on the OMC (Table 3). Further, this study illustrates the metal content, surface area, pore volume, and pore diameter of NiPd/OMC, Ni/OMC, Pd/OMC, and bare OMC.

Table 3. Characterization of each electrocatalysts.

	NiPd/OMC	Ni/OMC	Pd/OMC	Bare-OMC
Ni (wt%)	10	10	-	-
Pd (wt%)	10	-	10	-
Pore volume (cm ³ g ⁻¹)	0.91	1.17	1.26	1.45
Pore diameter (nm) ^a	5.3	5.3	5.2	5.3
Surface area (m ² g ⁻¹) ^b	862	1243	1078	1434

^a The pore diameters were calculated from desorption branches using BJH method. ^b The surface areas were obtained by the BET method.

The operating electrode was constructed by drop-coating the slurry mixture for electrochemical measurements. The arrangement of the electrochemical cells and the method of potential conversion from Ag/AgCl to RHE are the same as described elsewhere (Equation (1)):

$$E_{\text{RHE}} = E_{\text{Ag/AgCl}} + 0.059 \cdot \text{pH} + E^{\circ}_{\text{Ag/AgCl}} \quad (1)$$

The CV and LSV measurements were performed with 0.33 M urea in N₂ saturated 1 M KOH at the scanning frequencies 10 and 5 mV s⁻¹, respectively.

4.3. Results

XRD analysis was used to explore the crystalline structure of the NiPd/OMC, Pd/OMC, and Ni/OMC electrocatalysts (Figure 22a). The NiPd/OMC XRD pattern reflects that the two major characteristic peaks of the bimetallic NiPd alloy's fcc crystalline structures were clearly displayed and assigned (JCPDS no 01-072-2515). Furthermore, the scale of the bimetallic NiPd alloy NPs was measured to be as small as 1.6 nm using the Scherrer method. TEM and HRTEM produced NiPd alloy NPs found in OMC scale and distribution (Figure 22b,c). Figure 22b reveals the effective loading of flat, widely dispersed, and very low bimetallic NiPd NPs onto the OMC supply. The parallel lattice fringe corresponds to the (111) plane of large crystalline NiPd NPs, with a calculated spacing gap of 0.22 nm, as presented in Figure 22c.

In a tri-electrode system, all the experiments were performed to verify the electrocatalytic behavior of catalytic activity for CV, LSV, and CA in a 1 M KOH solution. The electrocatalytic activities for UOR of electrocatalysts like NiPd/OMC, Ni/OMC, Pd/OMC, and bare OMC were detected and compared with the IrO/C catalyst standard in the existence of 0.33 M urea in N₂-saturated 1 M KOH solution at a

scanning frequency of 5 mV s^{-1} (Figure 23a). In addition, their Tafel plots have often compared the UOR kinetics with the prepared electrocatalysts (Figure 23b). Therefore, the Tafel slope displayed the lowest NiPd/OMC of 31 mV dec^{-1} and Ni/OMC, Pd/OMC, and OMC of 36 , 59 , and 64 mV dec^{-1} , respectively, in the UOR and little lower than the IrO/C electrocatalyst. This result suggests that a smaller slope value of the Tafel NiPd/OMC electrocatalyst will result in better and faster catalytic kinetics on UOR. The essential factor in the catalytic activity is durability (Figure 23c). The NiPd/OMC electrocatalytic UOR performance displays an overpotential of 1.346 V vs. RHE required to achieve the current density. These remarkably strong catalytic activities, such as high current intensity, good conductivity, low overpotential, low Tafel performance, and good longevity of NiPd/OMC electrocatalysts, may be attributed to the following significant factors:

1. The existence of Ni^{3+} cationic active material at NiOOH enables effortless electron jumping mechanism and can also induce electrocatalytic reaction transmission.
2. OMC has very large surface area, pore volume, and pore diameters that may indicate higher UOR electroactive interfacial sites and ion/ e^- transfer speeds.

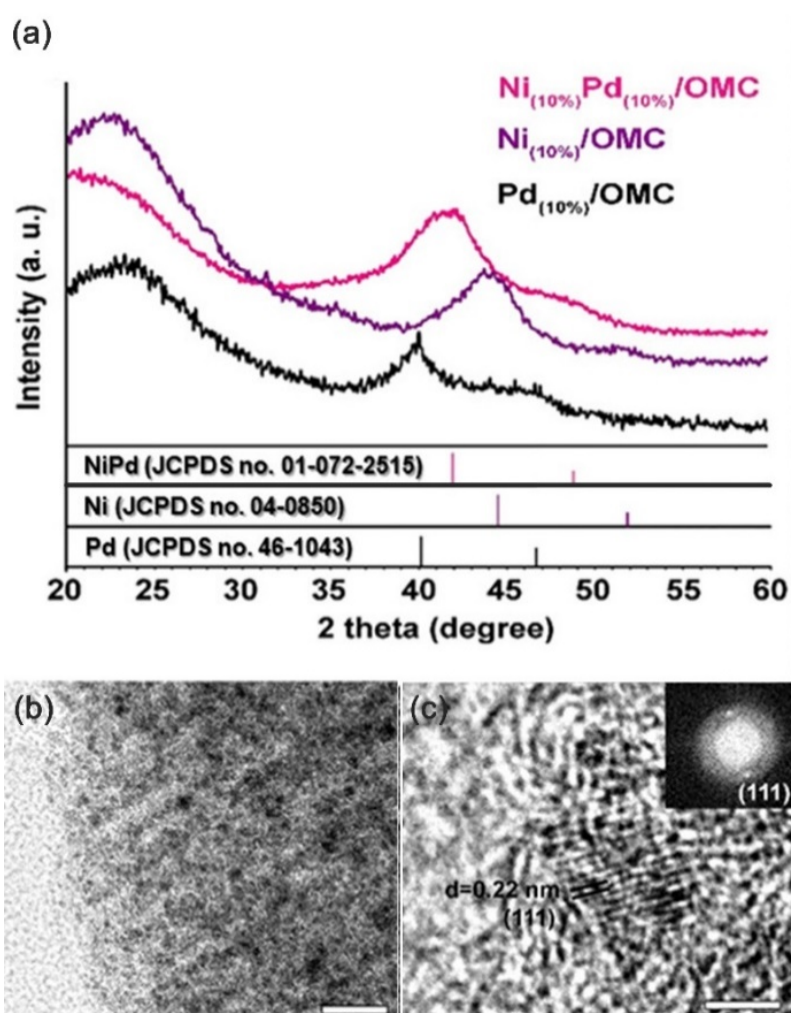


Figure 22. (a) XRD spectra of NiPd/OMC, Ni/OMC, and Pd/OMC. (b) TEM image, and (c) HRTEM image of NiPd/OMC nanocatalyst. The bars indicate 20 nm (b) and 2 nm (c). Reproduced and adapted from Ref. [200]; Copyright (2019), American Chemical Society.

In this review, the as-prepared electrocatalysts were also explored for observations of the HER in the N_2 -saturated 1 M KOH aqueous solution with and without 0.33 M urea solution. As depicted in

Figure 23d,e, the values of NiPd/OMC material electrocatalyst with respect to overpotential (-0.117 V vs. RHE) and Tafel slope suggests the extremely efficient and rapid HER kinetics. The Tafel slope value of 37 mV dec^{-1} for the NiPd/OMC electrocatalyst is based on familiar mechanisms for the electrocatalytic HER operation and suggests a Volmer–Heyrovsky mechanism [199]. The Tafel slopes of the electrocatalysts depicted in Figure 23e derived from the LSV polarization curves are estimated to be 29, 37, 65, 76, and 210 mV dec^{-1} for Pt@C, NiPd/OMC, Ni/OMC, Pd/OMC, and bare OMC, respectively. In fact, in the LSV polarization curves, a large decay of its HER behavior was not detected in between 5000 cycles, even after the 5000 period of CV operation (Figure 23f). Apart from the extremely good HER behavior in the N_2 -saturated 1 M KOH electrolyte with 0.33 M urea solution, the NiPd/OMC electrocatalyst was operated in the empty N_2 -saturated 1 M KOH electrolyte. Fortunately, no significant shifts in the intensity of cathodic current are seen in Figure 23f, indicating that the NiPd/OMC electrocatalyst has superior catalytic efficiency in both general water and urea electrolysis applications.

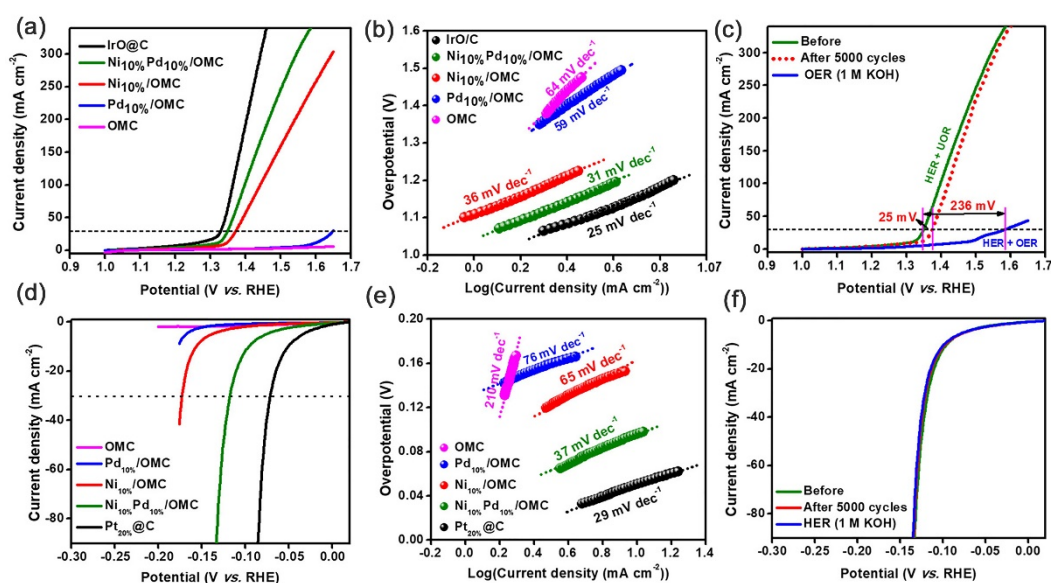


Figure 23. Urea oxidation reaction (UOR) electrocatalytic properties of IrO@C, NiPd/OMC, Ni/OMC, Pd/OMC, and OMC. (a) LSV plots, (b) respective Tafel plots derived from (a), (c) durability and OER analysis of NiPd/OMC performed without urea. HER electrocatalytic properties of Pt@C, NiPd/OMC, Ni/OMC, Pd/OMC, and OMC. (d) LSV plots, (e) respective Tafel plots derived from (d), and durability and HER analysis of NiPd/OMC. (f) durability and HER analysis of NiPd/OMC performed without and with 0.33 M urea in N_2 saturated 1 M KOH at scan rate = 5 mV s^{-1} . All of reaction performed in N_2 saturated 1 M KOH with 0.33 M urea at scan rate = 5 mV s^{-1} . Reproduced and adapted from Ref. [200]; Copyright (2019), American Chemical Society.

5. Conclusions

Herein we have reviewed effective catalysts in terms of their overall reaction to water splitting. In other words, the advantages that dictate the application of these materials as both cathodes and anodes indicate the direction in which hybrid materials are developed. The addition of defect sites, heterostructures, and heteroatom doping, which can be applied to such hybrid materials, indicates their potential for water splitting. Also, transition metal pnictides and chalcogenides using these strategies have displayed positive potentials toward HER and OER because of high conductivity and activity. In HER, heterostructure like Ni and Co hydroxides with 2D nanostructure like MoS_2 can show outstanding performance through efficient electron/mass transfer and optimized catalytic sites. In OER, transition metal pnictides and chalcogenides can display excellent catalytic activity with thin oxide layer on the catalysts surface. But there are several things to overcome despite much studies

and efforts. For example, it is significant to resist corrosion in electrolytes under high anodic potential without any phase transformation in OER, which is a problem directly related to the durability of the OER catalysts. In HER, even though electrocatalysts-based platinum or platinum alloys exhibit superior activity to Pt/C in alkaline solution, there was no noticeable decrease in Pt loading.

For a fundamental solution of these issues, understanding the mechanism of the reactions must be involved in order to perform synthesis of perfect electrocatalyst toward HER and OER. Catalysts development of in situ methods have many advantages in terms of easy understanding of the reaction mechanism and high stability. Substrates like metal foam such as Ni foam and NiCrAl foam or carbon cloth (CC) can be example of this approaches. Consequently, more methods which display enhanced activity for overall water splitting will be developed to synthesis heterostructure and transition metal complex with doping heteroatoms or defect sites for high conductivity on the substrate. Also, single atom nanocatalysts on substrates can suggest direction of lowering Pt loading toward HER and for minimizing phase transformation in OER, mixing the nanocompounds with other elements or depositing buffer layer can be solution to improve stability of catalysts on substrates. As a recent trend, beyond the limits of only electrochemical water splitting, photoelectrolysis can be considered as one of the environmental methods that exploits solar energy. This strategy will contribute to future energy field because it can present the synergistic effect of water splitting by smoothly moving electrons using solar energy which is unlimited energy. Notably, researches with theoretical calculations or computational results should be performed by processing fabrication electrocatalysts, which can accelerate provision of intrinsic knowledge of HER and OER. Furthermore, UOR, the method of generating electricity by decomposing materials such as urea, can also be implemented to solve environmental problems like air pollution and greenhouse effect. Our previous catalysts, e.g., NiPd/CMK-3 nanocatalyst for the electrocatalyst of UOR and HER activities, also exhibited good catalytic activities. It can be applied to HER because of the efficiency of Mo, Ni, and Co, but we can expect to apply it to different electrochemical reactions like ORR and OER in our next work. We also expect that our approach can be adapted in the near future for other catalytic syntheses.

Author Contributions: K.H.P. provided academic direction, conceptualization, validation, funding acquisition, writing—reviewing and editing. S.J. and K.M. contributed equally on that work. Specially, S.J. collected materials and wrote the introduction and conclusion part. K.M. contributed in results and discussion part and checked English style as well as grammatical errors throughout the manuscript. Y.P. and S.P. contributed to the materials and methods and results and discussion part. All authors have read and agreed to the published version of the manuscript.

Funding: This research was funded by 2-Year Research Grant of Pusan National University.

Acknowledgments: This work was supported by a 2-Year Research Grant of Pusan National University.

Conflicts of Interest: The authors declare no conflict of interest.

Abbreviations

NPs	nanoparticles
OER	oxygen evolution reaction
HER	hydrogen evolution reaction
ORR	oxygen reduction reaction
TMP	transition metal phosphide
LOB	lithium–oxygen batteries
CVD	chemical vapor deposition
ADF-STEM	atomic-resolution annular dark field-scanning transmission electron microscope
HAADF	high angle annular dark field
EDX	energy dispersive X-ray
PXRD	powder X-ray diffraction
Pa3	cubic pyrite-type phase
BET	Brunauer-Emmett-Teller
PBS	phosphate-buffered saline

NF	nickel foam
RHE	reversible hydrogen electrode
EIS	electrochemical impedance spectroscopy
CV	cyclic voltammetry
CA	chronoamperometry
LSV	linear sweep voltammetry
TMD	transition metal dichalcogenide
LDH	layered double hydroxide
DI	deionized
EDA	ethylene diamine
CC	carbon cloth
HRTEM	high-resolution transmission electron microscope
Pi	inorganic phosphate
XRD	X-ray diffraction
C _{dl}	double-layer capacitance
RFLB	rechargeable redox flow lithium battery
RFLOB	lithium-oxygen redox flow battery
GDT	gas diffusion tank
TMPPA	tris[4-[2-(2-methoxyethoxy)ethoxy]phenyl]amine
DTBBQ	2,5-di- <i>tert</i> -butyl- <i>p</i> -benzoquinone
RDE	rotating disk electrode
UOR	urea electro-oxidation reaction
OMC	ordered mesoporous carbon
BJH	Barrett-Joyner-Halenda
fcc	face centered cubic

References

1. Ghosh, T.; Mohammad, A.; Mobin, S.M. Hybrid Cobalt Doped-Cerium Oxide as a Multifunctional Nanocatalyst for Various Organic Transformations. *ACS Sustain. Chem. Eng.* **2019**, *7*, 13746–13763. [[CrossRef](#)]
2. Díaz, U.; Brunel, D.; Corma, A. Catalysis using Multifunctional Organosiliceous Hybrid Materials. *Chem. Soc. Rev.* **2013**, *42*, 4083–4097. [[CrossRef](#)] [[PubMed](#)]
3. Loy, D.A.; Shea, K.J. Bridged Polysilsesquioxanes. Highly Porous Hybrid Organic-Inorganic Materials. *Chem. Rev.* **1995**, *95*, 1431–1442. [[CrossRef](#)]
4. Di Carlo, G.; Lualdi, M.; Venezia, A.M.; Boutonnet, M.; Sanchez-Dominguez, M. Design of Cobalt Nanoparticles with Tailored Structural and Morphological Properties via O/W and W/O Microemulsions and Their Deposition onto Silica. *Catalysts* **2015**, *5*, 442–459. [[CrossRef](#)]
5. Jang, S.; Hira, S.A.; Annas, D.; Song, S.; Yusuf, M.; Park, J.C.; Park, S.; Park, K.H. Recent Novel Hybrid Pd-Fe₃O₄ Nanoparticles as Catalysts for Various C-C Coupling Reactions. *Processes* **2019**, *7*, 422–452. [[CrossRef](#)]
6. Tan, L.; Wu, X.; Chen, D.; Liu, H.; Meng, X.; Tang, F. Confining Alloy or Core-Shell Au-Pd Bimetallic Nanocrystals in Silica Nanorattles for Enhanced Catalytic Performance. *J. Mater. Chem. A* **2013**, *1*, 10382–10388. [[CrossRef](#)]
7. Moussa, S.; Siamaki, A.R.; Gupton, B.F.; El-Shall, M.S. Pd-Partially Reduced Graphene Oxide Catalysts (Pd/PRGO): Laser Synthesis of Pd Nanoparticles Supported on PRGO Nanosheets for Carbon-carbon Cross Coupling Reactions. *ACS Catal.* **2012**, *2*, 145–154. [[CrossRef](#)]
8. Nasrollahzadeh, M.; Mohammad Sajadi, S.; Rostami-Vartooni, A.; Khalaj, M. Green Synthesis of Pd/Fe₃O₄ Nanoparticles Using Euphorbia Condylcarpa M. Bieb Root Extract and Their Catalytic Applications as Magnetically Recoverable and Stable Recyclable Catalysts for the Phosphine-Free Sonogashira and Suzuki Coupling Reactions. *J. Mol. Catal. A Chem.* **2015**, *396*, 31–39. [[CrossRef](#)]
9. Siamaki, A.R.; Khder, A.E.R.S.; Abdelsayed, V.; El-Shall, M.S.; Gupton, B.F. Microwave-Assisted Synthesis of Palladium Nanoparticles Supported on Graphene: A Highly Active and Recyclable Catalyst for Carbon-Carbon Cross-Coupling Reactions. *J. Catal.* **2011**, *279*, 1–11. [[CrossRef](#)]

10. Truong, Q.D.; Le, T.S.; Ling, Y.C. Pt Deposited TiO₂ Catalyst Fabricated by Thermal Decomposition of Titanium Complex for Solar Hydrogen Production. *Solid State Sci.* **2014**, *38*, 18–24. [[CrossRef](#)]
11. Woo, H.; Lee, K.; Park, J.C.; Park, K.H. Facile Synthesis of Pd/Fe₃O₄/Charcoal Bifunctional Catalysts with High Metal Loading for High Product Yields in Suzuki-Miyaura Coupling Reactions. *New J. Chem.* **2014**, *38*, 5626–5632. [[CrossRef](#)]
12. Tan, Q.; Du, C.; Sun, Y.; Yin, G.; Gao, Y. Pd-around-CeO_{2-x} Hybrid Nanostructure Catalyst: Three-Phase-Transfer Synthesis, Electrocatalytic Properties and Dual Promoting Mechanism. *J. Mater. Chem. A* **2014**, *2*, 1429–1435. [[CrossRef](#)]
13. Hosseini, S.G.; Abazari, R.; Ghavi, A. Pure CuCr₂O₄ Nanoparticles: Synthesis, Characterization and Their Morphological and Size Effects on the Catalytic Thermal Decomposition of Ammonium Perchlorate. *Solid State Sci.* **2014**, *37*, 72–79. [[CrossRef](#)]
14. Veisi, H.; Sedrpoushan, A.; Maleki, B.; Hekmati, M.; Heidari, M.; Hemmati, S. Palladium Immobilized on Amidoxime-Functionalized Magnetic Fe₃O₄ Nanoparticles: A Highly Stable and Efficient Magnetically Recoverable Nanocatalyst for Sonogashira Coupling Reaction. *Appl. Organomet. Chem.* **2015**, *29*, 834–839. [[CrossRef](#)]
15. Wang, D.; Li, Y. One-Pot Protocol for Au-Based Hybrid Magnetic Nanostructures via a Noble-Metal-Induced Reduction Process. *J. Am. Chem. Soc.* **2010**, *132*, 6280–6281. [[CrossRef](#)]
16. Jin, X.; Dang, L.; Lohrman, J.; Subramaniam, B.; Ren, S.; Chaudhari, R.V. Lattice-Matched Bimetallic CuPd-Graphene Nanocatalysts for Facile Conversion of Biomass-Derived Polyols to Chemicals. *ACS Nano* **2013**, *7*, 1309–1316. [[CrossRef](#)]
17. Dong, B.; Miller, D.L.; Li, C.Y. Polymer Single Crystal as Magnetically Recoverable Support for Nanocatalysts. *J. Phys. Chem. Lett.* **2012**, *3*, 1346–1350. [[CrossRef](#)]
18. Omar, S.; Abu-Reziq, R. Palladium Nanoparticles Supported on Magnetic Organic-Silica Hybrid Nanoparticles. *J. Phys. Chem. C* **2014**, *118*, 30045–30056. [[CrossRef](#)]
19. Hu, H.; Xin, J.H.; Hu, H.; Wang, X.; Miao, D.; Liu, Y. Synthesis and Stabilization of Metal Nanocatalysts for Reduction Reactions—A Review. *J. Mater. Chem. A* **2015**, *3*, 11157–11182. [[CrossRef](#)]
20. Askari, S.; Halladj, R.; Azarhoosh, M.J. Modeling and Optimization of Catalytic Performance of SAPO-34 Nanocatalysts Synthesized Sonochemically using a New Hybrid of Non-Dominated Sorting Genetic Algorithm-II based Artificial Neural Networks (NSGA-II-ANNs). *RSC Adv.* **2015**, *5*, 52788–52800. [[CrossRef](#)]
21. Zheng, Y.; Chen, C.; Zhan, Y.; Lin, X.; Zheng, Q.; Wei, K.; Zhu, J. Photocatalytic Activity of Ag/ZnO Heterostructure Nanocatalyst: Correlation between Structure and Property. *J. Phys. Chem. C* **2008**, *112*, 10773–10777. [[CrossRef](#)]
22. Sharma, R.K.; Sharma, S.; Dutta, S.; Zboril, R.; Gawande, M.B. Silica-Nanosphere-Based Organic-Inorganic Hybrid Nanomaterials: Synthesis, Functionalization and Applications in Catalysis. *Green Chem.* **2015**, *17*, 3207–3230. [[CrossRef](#)]
23. Song, H. Metal Hybrid Nanoparticles for Catalytic Organic and Photochemical Transformations. *Acc. Chem. Res.* **2015**, *48*, 491–499. [[CrossRef](#)] [[PubMed](#)]
24. Guo, L.T.; Cai, Y.Y.; Ge, J.M.; Zhang, Y.N.; Gong, L.H.; Li, X.H.; Wang, K.X.; Ren, Q.Z.; Su, J.; Chen, J.S. Multifunctional Au-Co@CN Nanocatalyst for Highly Efficient Hydrolysis of Ammonia Borane. *ACS Catal.* **2015**, *5*, 388–392. [[CrossRef](#)]
25. Kim, S.M.; Lee, S.J.; Kim, S.H.; Kwon, S.; Yee, K.J.; Song, H.; Somorjai, G.A.; Park, J.Y. Hot Carrier-Driven Catalytic Reactions on Pt-CdSe-Pt Nanodumbbells and Pt/GaN under Light Irradiation. *Nano Lett.* **2013**, *13*, 1352–1358. [[CrossRef](#)]
26. Tollefson, J. Fuel of the Future? *Automot. Eng. Int.* **1977**, *85*, 48–52.
27. Chu, S.; Majumdar, A. Opportunities and Challenges for a Sustainable Energy Future. *Nature* **2012**, *488*, 294–303. [[CrossRef](#)]
28. Seh, Z.W.; Kibsgaard, J.; Dickens, C.F.; Chorkendorff, I.; Nørskov, J.K.; Jaramillo, T.F. Combining Theory and Experiment in Electrocatalysis: Insights into Materials Design. *Science* **2017**, *355*, 146–157. [[CrossRef](#)]
29. Stamenkovic, V.R.; Strmcnik, D.; Lopes, P.P.; Markovic, N.M. Energy and Fuels from Electrochemical Interfaces. *Nat. Mater.* **2016**, *16*, 57–69. [[CrossRef](#)]
30. Greeley, J.; Jaramillo, T.F.; Bonde, J.; Chorkendorff, I.; Nørskov, J.K. Computational High-Throughput Screening of Electrocatalytic Materials for Hydrogen Evolution. *Nat. Mater.* **2006**, *5*, 909–913. [[CrossRef](#)]

31. Gao, M.R.; Xu, Y.F.; Jiang, J.; Yu, S.H. Nanostructured Metal Chalcogenides: Synthesis, Modification, and Applications in Energy Conversion and Storage Devices. *Chem. Soc. Rev.* **2013**, *42*, 2986–3017. [[CrossRef](#)] [[PubMed](#)]
32. Gao, M.R.; Liang, J.X.; Zheng, Y.R.; Xu, Y.F.; Jiang, J.; Gao, Q.; Li, J.; Yu, S.H. An Efficient Molybdenum Disulfide/Cobalt Diselenide Hybrid Catalyst for Electrochemical Hydrogen Generation. *Nat. Commun.* **2015**, *6*, 1–7. [[CrossRef](#)] [[PubMed](#)]
33. Walter, M.G.; Warren, E.L.; McKone, J.R.; Boettcher, S.W.; Mi, Q.; Santori, E.A.; Lewis, N.S. Solar Water Splitting Cells. *Chem. Rev.* **2010**, *110*, 6446–6473. [[CrossRef](#)] [[PubMed](#)]
34. Cook, T.R.; Dogutan, D.K.; Reece, S.Y.; Surendranath, Y.; Teets, T.S.; Nocera, D.G. Solar Energy Supply and Storage for the Legacy and Nonlegacy Worlds. *Chem. Rev.* **2010**, *110*, 6474–6502. [[CrossRef](#)] [[PubMed](#)]
35. Chen, W.F.; Muckerman, J.T.; Fujita, E. Recent Developments in Transition metal Carbides and Nitrides as Hydrogen Evolution Electrocatalysts. *Chem. Commun.* **2013**, *49*, 8896–8909. [[CrossRef](#)]
36. Matsumoto, Y.; Sato, E. Electrocatalytic Properties of Transition Metal Oxides for Oxygen Evolution Reaction. *Mater. Chem. Phys.* **1986**, *14*, 397–426. [[CrossRef](#)]
37. Jaramillo, T.F.; Ivanovskaya, A.; McFarland, E.W. High-Throughput Screening System for Catalytic Hydrogen-Producing Materials. *J. Comb. Chem.* **2002**, *4*, 17–22. [[CrossRef](#)]
38. Chen, G.; Delafuente, D.A.; Sarangapani, S.; Mallouk, T.E. Combinatorial Discovery of Bifunctional Oxygen Reduction - Water Oxidation Electrocatalysts for Regenerative Fuel Cells. *Catal. Today* **2001**, *67*, 341–355. [[CrossRef](#)]
39. Gerken, J.B.; Chen, J.Y.C.; Massé, R.C.; Powell, A.B.; Stahl, S.S. Development of an O₂-Sensitive Fluorescence-Quenching Assay for the Combinatorial Discovery of Electrocatalysts for Water Oxidation. *Angew. Chem. Int. Ed.* **2012**, *51*, 6676–6680. [[CrossRef](#)]
40. Liu, X.; Shen, Y.; Yang, R.; Zou, S.; Ji, X.; Shi, L.; Zhang, Y.; Liu, D.; Xiao, L.; Zheng, X.; et al. Inkjet Printing Assisted Synthesis of Multicomponent Mesoporous Metal Oxides for Ultrafast Catalyst Exploration. *Nano Lett.* **2012**, *12*, 5733–5739. [[CrossRef](#)]
41. Gregoire, J.M.; Xiang, C.; Mitrovic, S.; Liu, X.; Marcin, M.; Cornell, E.W.; Fan, J.; Jin, J. Combined Catalysis and Optical Screening for High Throughput Discovery of Solar Fuels Catalysts. *J. Electrochem. Soc.* **2013**, *160*, F337–F342. [[CrossRef](#)]
42. Seley, D.; Ayers, K.; Parkinson, B.A. Combinatorial Search for Improved Metal Oxide Oxygen Evolution Electrocatalysts in Acidic Electrolytes. *ACS Comb. Sci.* **2013**, *15*, 82–89. [[CrossRef](#)] [[PubMed](#)]
43. Berglund, S.P.; Lee, H.C.; Núñez, P.D.; Bard, A.J.; Mullins, C.B. Screening of Transition and Post-Transition Metals to Incorporate into Copper Oxide and Copper Bismuth Oxide for Photoelectrochemical Hydrogen Evolution. *Phys. Chem. Chem. Phys.* **2013**, *15*, 4554–4565. [[CrossRef](#)] [[PubMed](#)]
44. Lu, Q.; Wang, A.L.; Cheng, H.; Gong, Y.; Yun, Q.; Yang, N.; Li, B.; Chen, B.; Zhang, Q.; Zong, Y.; et al. Synthesis of Hierarchical 4H/fcc Ru Nanotubes for Highly Efficient Hydrogen Evolution in Alkaline Media. *Small* **2018**, *14*, 1–5. [[CrossRef](#)]
45. Tian, H.; Cui, X.; Zeng, L.; Su, L.; Song, Y.; Shi, J. Oxygen Vacancy-Assisted Hydrogen Evolution Reaction of the Pt/WO₃ Electrocatalyst. *J. Mater. Chem. A* **2019**, *7*, 6285–6293. [[CrossRef](#)]
46. Zheng, Y.; Jiao, Y.; Zhu, Y.; Li, L.H.; Han, Y.; Chen, Y.; Jaroniec, M.; Qiao, S.Z. High Electrocatalytic Hydrogen Evolution Activity of an Anomalous Ruthenium Catalyst. *J. Am. Chem. Soc.* **2016**, *138*, 16174–16181. [[CrossRef](#)]
47. Yang, Y.; Wang, S.; Zhang, J.; Li, H.; Tang, Z.; Wang, X. Nanosheet-Assembled MoSe₂ and S-doped MoSe_{2-x} Nanostructures for Superior Lithium Storage Properties and Hydrogen Evolution Reactions. *Inorg. Chem. Front.* **2015**, *2*, 931–937. [[CrossRef](#)]
48. Peng, S.; Li, L.; Tan, H.; Cai, R.; Shi, W.; Li, C.; Mhaisalkar, S.G.; Srinivasan, M.; Ramakrishna, S.; Yan, Q. MS₂ (M = Co and Ni) Hollow Spheres with Tunable Interiors for High-Performance Supercapacitors and Photovoltaics. *Adv. Funct. Mater.* **2014**, *24*, 2155–2162. [[CrossRef](#)]
49. Lu, X.F.; Yu, L.; Lou, X.W. Highly Crystalline Ni-Doped FeP/Carbon Hollow Nanorods as all-pH Efficient and Durable Hydrogen Evolving Electrocatalysts. *Sci. Adv.* **2019**, *5*, 1–10. [[CrossRef](#)]
50. Hao, W.; Wu, R.; Zhang, R.; Ha, Y.; Chen, Z.; Wang, L.; Yang, Y.; Ma, X.; Sun, D.; Fang, F.; et al. Electroless Plating of Highly Efficient Bifunctional Boride-Based Electrodes toward Practical Overall Water Splitting. *Adv. Energy Mater.* **2018**, *8*, 1–7. [[CrossRef](#)]

51. Ha, Y.; Shi, L.; Chen, Z.; Wu, R. Phase-Transited Lysozyme-Driven Formation of Self-Supported $\text{Co}_3\text{O}_4@\text{C}$ Nanomeshes for Overall Water Splitting. *Adv. Sci.* **2019**, *6*, 1–8.
52. Chen, Z.; Ha, Y.; Liu, Y.; Wang, H.; Yang, H.; Xu, H.; Li, Y.; Wu, R. In Situ Formation of Cobalt Nitrides/Graphitic Carbon Composites as Efficient Bifunctional Electrocatalysts for Overall Water Splitting. *ACS Appl. Mater. Interfaces* **2018**, *10*, 7134–7144. [[CrossRef](#)] [[PubMed](#)]
53. Liu, P.; Rodriguez, J.A. Catalysts for Hydrogen Evolution from the [NiFe] Hydrogenase to the $\text{Ni}_2\text{P}(001)$ Surface: The Importance of Ensemble Effect. *J. Am. Chem. Soc.* **2005**, *127*, 14871–14878. [[CrossRef](#)]
54. Görlin, M.; Chernev, P.; De Araújo, J.F.; Reier, T.; Dresch, S.; Paul, B.; Krähnert, R.; Dau, H.; Strasser, P. Oxygen Evolution Reaction Dynamics, Faradaic Charge Efficiency, and the Active Metal Redox States of Ni-Fe Oxide Water Splitting Electrocatalysts. *J. Am. Chem. Soc.* **2016**, *138*, 5603–5614. [[CrossRef](#)] [[PubMed](#)]
55. Zhu, Y.P.; Liu, Y.P.; Ren, T.Z.; Yuan, Z.Y. Self-Supported Cobalt Phosphide Mesoporous Nanorod Arrays: A Flexible and Bifunctional Electrode for Highly Active Electrocatalytic Water Reduction and Oxidation. *Adv. Funct. Mater.* **2015**, *25*, 7337–7347. [[CrossRef](#)]
56. Carencu, S.; Portehault, D.; Boissière, C.; Mézailles, N.; Sanchez, C. Nanoscaled Metal Borides and Phosphides: Recent Developments and Perspectives. *Chem. Rev.* **2013**, *113*, 7981–8065. [[CrossRef](#)]
57. Shi, Y.; Zhang, B. Recent Advances in Transition Metal Phosphide Nanomaterials: Synthesis and Applications in Hydrogen Evolution Reaction. *Chem. Soc. Rev.* **2016**, *45*, 1529–1541. [[CrossRef](#)]
58. Zhang, R.; Huang, J.; Chen, G.; Chen, W.; Song, C.; Li, C.; Ostrikov, K. In Situ Engineering Bi-Metallic Phospho-Nitride Bi-Functional Electrocatalysts for Overall Water Splitting. *Appl. Catal. B Environ.* **2019**, *254*, 414–423. [[CrossRef](#)]
59. Wu, R.; Wang, D.P.; Zhou, K.; Srikanth, N.; Wei, J.; Chen, Z. Porous Cobalt Phosphide/Graphitic Carbon Polyhedral Hybrid Composites for Efficient Oxygen Evolution Reactions. *J. Mater. Chem. A* **2016**, *4*, 13742–13745. [[CrossRef](#)]
60. Lin, Y.; Pan, Y.; Liu, S.; Sun, K.; Cheng, Y.; Liu, M.; Wang, Z.; Li, X.; Zhang, J. Construction of Multi-Dimensional Core/Shell Ni/NiCoP Nano-Heterojunction for Efficient Electrocatalytic Water Splitting. *Appl. Catal. B Environ.* **2019**, *259*, 118036–118039. [[CrossRef](#)]
61. Li, J.S.; Kong, L.X.; Wu, Z.; Zhang, S.; Yang, X.Y.; Sha, J.Q.; Liu, G.D. Polydopamine-Assisted Construction of Cobalt Phosphide Encapsulated in N-Doped Carbon Porous Polyhedrons for Enhanced Overall Water Splitting. *Carbon* **2019**, *145*, 694–700. [[CrossRef](#)]
62. Dutta, S.; Indra, A.; Han, H.S.; Song, T. An Intriguing Pea-Like Nanostructure of Cobalt Phosphide on Molybdenum Carbide Incorporated Nitrogen-Doped Carbon Nanosheets for Efficient Electrochemical Water Splitting. *ChemSusChem* **2018**, *11*, 3956–3964. [[CrossRef](#)] [[PubMed](#)]
63. Hoa, V.H.; Tran, D.T.; Le, H.T.; Kim, N.H.; Lee, J.H. Hierarchically Porous Nickel–Cobalt Phosphide Nanoneedle Arrays Loaded Micro-Carbon Spheres as an Advanced Electrocatalyst for Overall Water Splitting Application. *Appl. Catal. B Environ.* **2019**, *253*, 235–245. [[CrossRef](#)]
64. Xu, H.; Jia, H.; Fei, B.; Ha, Y.; Li, H.; Guo, Y.; Liu, M.; Wu, R. Charge Transfer Engineering via Multiple Heteroatom Doping in Dual Carbon-Coupled Cobalt Phosphides for Highly Efficient Overall Water Splitting. *Appl. Catal. B Environ.* **2020**, *268*, 118404–118412. [[CrossRef](#)]
65. Lin, H.; Shi, Z.; He, S.; Yu, X.; Wang, S.; Gao, Q.; Tang, Y. Heteronanowires of $\text{MoC-Mo}_2\text{C}$ as Efficient Electrocatalysts for Hydrogen Evolution Reaction. *Chem. Sci.* **2016**, *7*, 3399–3405. [[CrossRef](#)]
66. Wang, D.; Li, Q.; Han, C.; Xing, Z.; Yang, X. When NiO@Ni Meets WS_2 Nanosheet Array: A Highly Efficient and Ultrastable Electrocatalyst for Overall Water Splitting. *ACS Cent. Sci.* **2018**, *4*, 112–119. [[CrossRef](#)]
67. Rui, K.; Zhao, G.; Chen, Y.; Lin, Y.; Zhou, Q.; Chen, J.; Zhu, J.; Sun, W.; Huang, W.; Dou, S.X. Hybrid 2D Dual-Metal–Organic Frameworks for Enhanced Water Oxidation Catalysis. *Adv. Funct. Mater.* **2018**, *28*, 1–9. [[CrossRef](#)]
68. Dou, S.; Wu, J.; Tao, L.; Shen, A.; Huo, J.; Wang, S. Carbon-Coated MoS_2 Nanosheets as Highly Efficient Electrocatalysts for the Hydrogen Evolution Reaction. *Nanotechnology* **2016**, *27*, 1–6. [[CrossRef](#)]
69. Chen, Y.; Zhou, Q.; Zhao, G.; Yu, Z.; Wang, X.; Dou, S.X.; Sun, W. Electrochemically Inert $\text{g-C}_3\text{N}_4$ Promotes Water Oxidation Catalysis. *Adv. Funct. Mater.* **2018**, *28*, 1–7.
70. Zhao, G.; Rui, K.; Dou, S.X.; Sun, W. Heterostructures for Electrochemical Hydrogen Evolution Reaction: A Review. *Adv. Funct. Mater.* **2018**, *28*, 1–26. [[CrossRef](#)]
71. Gupta, S.; Kellogg, W.; Xu, H.; Liu, X.; Cho, J.; Wu, G. Bifunctional Perovskite Oxide Catalysts for Oxygen Reduction and Evolution in Alkaline Media. *Chem. Asian J.* **2016**, *11*, 10–21. [[CrossRef](#)] [[PubMed](#)]

72. Abraham, K.M.; Jiang, Z. ELECTROCHEMICAL SCIENCE AND TECHNOLOGY A Polymer Electrolyte-Based Rechargeable Lithium/Oxygen Battery. *J. Electrochem. Soc.* **1996**, *143*, 1–5. [[CrossRef](#)]
73. Bruce, P.G.; Freunberger, S.A.; Hardwick, L.J.; Tarascon, J.M. Li-O₂ and Li-S Batteries with High Energy Storage. *Nat. Mater.* **2012**, *11*, 19–29. [[CrossRef](#)] [[PubMed](#)]
74. Jin, H.; Guo, C.; Liu, X.; Liu, J.; Vasileff, A.; Jiao, Y.; Zheng, Y.; Qiao, S.Z. Emerging Two-Dimensional Nanomaterials for Electrocatalysis. *Chem. Rev.* **2018**, *118*, 6337–6408. [[CrossRef](#)] [[PubMed](#)]
75. Urbańczyk, E.; Sowa, M.; Simka, W. Urea Removal from Aqueous Solutions—A Review. *J. Appl. Electrochem.* **2016**, *46*, 1011–1029. [[CrossRef](#)]
76. Xu, W.; Zhang, H.; Li, G.; Wu, Z. Nickel-Cobalt Bimetallic Anode Catalysts for Direct Urea Fuel Cell. *Sci. Rep.* **2014**, *4*, 1–6. [[CrossRef](#)]
77. Zhu, B.; Liang, Z.; Zou, R. Designing Advanced Catalysts for Energy Conversion Based on Urea Oxidation Reaction. *Small* **2020**, *16*, 1906133. [[CrossRef](#)]
78. Xie, J.; Yang, X.; Xie, Y. Defect Engineering in Two-Dimensional Electrocatalysts for Hydrogen Evolution. *Nanoscale* **2020**, *12*, 4238–4294. [[CrossRef](#)]
79. Lee, J.; Kim, C.; Choi, K.S.; Seo, J.; Choi, Y.; Choi, W.; Kim, Y.M.; Jeong, H.Y.; Lee, J.H.; Kim, G.; et al. In-Situ Coalesced Vacancies on MoSe₂ Mimicking Noble Metal: Unprecedented TAFEL Reaction in Hydrogen Evolution. *Nano Energy* **2019**, *63*, 103844–1038446. [[CrossRef](#)]
80. Shu, H.; Zhou, D.; Li, F.; Cao, D.; Chen, X. Defect Engineering in MoSe₂ for the Hydrogen Evolution Reaction: From Point Defects to Edges. *ACS Appl. Mater. Interfaces* **2017**, *9*, 42688–42698. [[CrossRef](#)]
81. He, J.; Zou, Y.; Wang, S. Defect Engineering on Electrocatalysts for Gas-Evolving Reactions. *Dalton Trans.* **2019**, *48*, 15–20. [[CrossRef](#)] [[PubMed](#)]
82. Zhang, H.; Zhang, J.; Li, Y.; Jiang, H.; Jiang, H.; Li, C. Continuous Oxygen Vacancy Engineering of the Co₃O₄ Layer for an Enhanced Alkaline Electrocatalytic Hydrogen Evolution Reaction. *J. Mater. Chem. A* **2019**, *7*, 13506–13510. [[CrossRef](#)]
83. Liu, T.; Feng, Z.; Li, Q.; Yang, J.; Li, C.; Dupuis, M. Role of Oxygen Vacancies on Oxygen Evolution Reaction Activity: β-Ga₂O₃ as a Case Study. *Chem. Mater.* **2018**, *30*, 7714–7726. [[CrossRef](#)]
84. Hirai, S.; Morita, K.; Yasuoka, K.; Shibuya, T.; Tojo, Y.; Kamihara, Y.; Miura, A.; Suzuki, H.; Ohno, T.; Matsuda, T.; et al. Oxygen Vacancy-Originated Highly Active Electrocatalysts for the Oxygen Evolution Reaction. *J. Mater. Chem. A* **2018**, *6*, 15102–15109. [[CrossRef](#)]
85. Li, H.; Tsai, C.; Koh, A.L.; Cai, L.; Contryman, A.W.; Fragapane, A.H.; Zhao, J.; Han, H.S.; Manoharan, H.C.; Abild-Pedersen, F.; et al. Activating and Optimizing MoS₂ Basal Planes for Hydrogen Evolution through the Formation of Strained Sulphur Vacancies. *Nat. Mater.* **2016**, *15*, 48–53. [[CrossRef](#)]
86. Ye, G.; Gong, Y.; Lin, J.; Li, B.; He, Y.; Pantelides, S.T.; Zhou, W.; Vajtai, R.; Ajayan, P.M. Defects Engineered Monolayer MoS₂ for Improved Hydrogen Evolution Reaction. *Nano Lett.* **2016**, *16*, 1097–1103. [[CrossRef](#)]
87. Tsai, C.; Li, H.; Park, S.; Park, J.; Han, H.S.; Nørskov, J.K.; Zheng, X.; Abild-Pedersen, F. Electrochemical Generation of Sulfur Vacancies in the Basal Plane of MoS₂ for Hydrogen Evolution. *Nat. Commun.* **2017**, *8*, 1–8. [[CrossRef](#)]
88. Li, B.; Gong, Y.; Hu, Z.; Brunetto, G.; Yang, Y.; Ye, G.; Zhang, Z.; Lei, S.; Jin, Z.; Bianco, E.; et al. Solid–Vapor Reaction Growth of Transition-Metal Dichalcogenide Monolayers. *Angew. Chem. Int. Ed.* **2016**, *55*, 1–7.
89. Shaw, J.C.; Zhou, H.; Chen, Y.; Weiss, N.O.; Liu, Y.; Huang, Y.; Duan, X. Chemical Vapor Deposition Growth of Monolayer MoSe₂ Nanosheets. *Nano Res.* **2014**, *7*, 1–7. [[CrossRef](#)]
90. Mahmood, J.; Li, F.; Jung, S.M.; Okyay, M.S.; Ahmad, I.; Kim, S.J.; Park, N.; Jeong, H.Y.; Baek, J.B. An Efficient and pH-Universal Ruthenium-Based Catalyst for the Hydrogen Evolution Reaction. *Nat. Nanotechnol.* **2017**, *12*, 441–446. [[CrossRef](#)]
91. Wang, D.; Zhang, X.; Bao, S.; Zhang, Z.; Fei, H.; Wu, Z. Phase Engineering of a Multiphase 1T/2H MoS₂ Catalyst for Highly Efficient Hydrogen Evolution. *J. Mater. Chem. A* **2017**, *5*, 2681–2688. [[CrossRef](#)]
92. Jiang, M.; Zhang, J.; Wu, M.; Jian, W.; Xue, H.; Ng, T.W.; Lee, C.S.; Xu, J. Synthesis of 1T-MoSe₂ Ultrathin Nanosheets with an Expanded Interlayer Spacing of 1.17 nm for Efficient Hydrogen Evolution Reaction. *J. Mater. Chem. A* **2016**, *4*, 14949–14953. [[CrossRef](#)]
93. Xu, C.; Peng, S.; Tan, C.; Ang, H.; Tan, H.; Zhang, H.; Yan, Q. Ultrathin S-Doped MoSe₂ Nanosheets for Efficient Hydrogen Evolution. *J. Mater. Chem. A* **2014**, *2*, 5597–5601. [[CrossRef](#)]

94. Shi, Y.; Zhou, Y.; Yang, D.R.; Xu, W.X.; Wang, C.; Wang, F.B.; Xu, J.J.; Xia, X.H.; Chen, H.Y. Energy Level Engineering of MoS₂ by Transition-Metal Doping for Accelerating Hydrogen Evolution Reaction. *J. Am. Chem. Soc.* **2017**, *139*, 15479–15485. [[CrossRef](#)] [[PubMed](#)]
95. Liu, B.; Zhang, L.; Xiong, W.; Ma, M. Cobalt-Nanocrystal-Assembled Hollow Nanoparticles for Electrocatalytic Hydrogen Generation from Neutral-pH Water. *Angew. Chem. Int. Ed.* **2016**, *55*, 6725–6729. [[CrossRef](#)]
96. Xu, K.; Cheng, H.; Liu, L.; Lv, H.; Wu, X.; Wu, C.; Xie, Y. Promoting Active Species Generation by Electrochemical Activation in Alkaline Media for Efficient Electrocatalytic Oxygen Evolution in Neutral Media. *Nano Lett.* **2017**, *17*, 578–583. [[CrossRef](#)]
97. Zheng, G.; Peng, Z.; Jia, D.; Al-Enizi, A.M.; Elzatahry, A.A. From Water Oxidation to Reduction: Homologous Ni-Co Based Nanowires as Complementary Water Splitting Electrocatalysts. *Adv. Energy Mater.* **2015**, *5*, 1–7.
98. Huang, Z.F.; Song, J.; Li, K.; Tahir, M.; Wang, Y.T.; Pan, L.; Wang, L.; Zhang, X.; Zou, J.J. Hollow Cobalt-Based Bimetallic Sulfide Polyhedra for Efficient All-pH-Value Electrochemical and Photocatalytic Hydrogen Evolution. *J. Am. Chem. Soc.* **2016**, *138*, 1359–1365. [[CrossRef](#)]
99. Boppella, R.; Tan, J.; Yang, W.; Moon, J. Homologous CoP/NiCoP Heterostructure on N-Doped Carbon for Highly Efficient and pH-Universal Hydrogen Evolution Electrocatalysis. *Adv. Funct. Mater.* **2019**, *29*, 1–9. [[CrossRef](#)]
100. Zou, X.; Huang, X.; Goswami, A.; Silva, R.; Sathe, B.R.; Mikmeková, E.; Asefa, T. Cobalt-embedded nitrogen-rich carbon nanotubes efficiently catalyze hydrogen evolution reaction at all pH values. *Angew. Chem. Int. Ed.* **2014**, *53*, 4372–4376. [[CrossRef](#)]
101. Xie, L.; Zhang, R.; Cui, L.; Liu, D.; Hao, S.; Ma, Y.; Du, G.; Asiri, A.M.; Sun, X. High-Performance Electrolytic Oxygen Evolution in Neutral Media Catalyzed by a Cobalt Phosphate Nanoarray. *Angew. Chem. Int. Ed.* **2017**, *56*, 1064–1068. [[CrossRef](#)]
102. Tian, J.; Liu, Q.; Asiri, A.M.; Sun, X. Self-Supported Nanoporous Cobalt Phosphide Nanowire Arrays: An Efficient 3D Hydrogen-Evolving Cathode over the Wide Range of pH 0–14. *J. Am. Chem. Soc.* **2014**, *136*, 7587–7590. [[CrossRef](#)]
103. Tabassum, H.; Guo, W.; Meng, W.; Mahmood, A.; Zhao, R.; Wang, Q.; Zou, R. Metal–Organic Frameworks Derived Cobalt Phosphide Architecture Encapsulated into B/N Co-Doped Graphene Nanotubes for All pH Value Electrochemical Hydrogen Evolution. *Adv. Energy Mater.* **2017**, *7*, 1–7. [[CrossRef](#)]
104. Liu, Y.; Xiao, C.; Lyu, M.; Lin, Y.; Cai, W.; Huang, P.; Tong, W.; Zou, Y.; Xie, Y. Ultrathin Co₃S₄ Nanosheets that Synergistically Engineer Spin States and Exposed Polyhedra that Promote Water Oxidation under Neutral Conditions. *Angew. Chem. Int. Ed.* **2015**, *54*, 11231–11235. [[CrossRef](#)] [[PubMed](#)]
105. Anantharaj, S.; Kennedy, J.; Kundu, S. Microwave-Initiated Facile Formation of Ni₃Se₄ Nanoassemblies for Enhanced and Stable Water Splitting in Neutral and Alkaline Media. *ACS Appl. Mater. Interfaces* **2017**, *9*, 8714–8728. [[CrossRef](#)] [[PubMed](#)]
106. Wang, Y.; Cui, X.; Zhao, J.; Jia, G.; Gu, L.; Zhang, Q.; Meng, L.; Shi, Z.; Zheng, L.; Wang, C.; et al. Rational Design of Fe-N/C Hybrid for Enhanced Nitrogen Reduction Electrocatalysis under Ambient Conditions in Aqueous Solution. *ACS Catal.* **2019**, *9*, 336–344. [[CrossRef](#)]
107. Zhang, G.; Feng, Y.S.; Lu, W.T.; He, D.; Wang, C.Y.; Li, Y.K.; Wang, X.Y.; Cao, F.F. Enhanced Catalysis of Electrochemical Overall Water Splitting in Alkaline Media by Fe Doping in Ni₃S₂ Nanosheet Arrays. *ACS Catal.* **2018**, *8*, 5431–5441. [[CrossRef](#)]
108. Cheng, N.; Liu, Q.; Asiri, A.M.; Xing, W.; Sun, X. A Fe-Doped Ni₃S₂ Particle Film as a High-Efficiency Robust Oxygen Evolution Electrode with very High Current Density. *J. Mater. Chem. A* **2015**, *3*, 23207–23212. [[CrossRef](#)]
109. Roger, I.; Shipman, M.A.; Symes, M.D. Earth-Abundant Catalysts for Electrochemical and Photoelectrochemical Water Splitting. *Nat. Rev. Chem.* **2017**, *1*, 1–13. [[CrossRef](#)]
110. Zhou, H.; Yu, F.; Huang, Y.; Sun, J.; Zhu, Z.; Nielsen, R.J.; He, R.; Bao, J.; Goddard, W.A.; Chen, S.; et al. Efficient Hydrogen Evolution by Ternary Molybdenum Sulfoselenide Particles on Self-Standing Porous Nickel Diselenide Foam. *Nat. Commun.* **2016**, *7*, 1–7. [[CrossRef](#)]
111. Xie, D.; Tang, W.; Wang, Y.; Xia, X.; Zhong, Y.; Zhou, D.; Wang, D.; Wang, X.; Tu, J. Facile Fabrication of Integrated Three-Dimensional C-MoSe₂/Reduced Graphene Oxide Composite with Enhanced Performance for Sodium Storage. *Nano Res.* **2016**, *9*, 1618–1629. [[CrossRef](#)]

112. Zhou, H.; Yu, F.; Sun, J.; Zhu, H.; Mishra, I.K.; Chen, S.; Ren, Z. Highly Efficient Hydrogen Evolution from Edge-Oriented $WS_{2(1-x)}Se_{2x}$ Particles on Three-Dimensional Porous $NiSe_2$ Foam. *Nano Lett.* **2016**, *16*, 7604–7609. [[CrossRef](#)] [[PubMed](#)]
113. Xu, K.; Wang, F.; Wang, Z.; Zhan, X.; Wang, Q.; Cheng, Z.; Safdar, M.; He, J. Component-Controllable $WS_{2(1-x)}Se_{2x}$ Nanotubes for Efficient Hydrogen Evolution Reaction. *ACS Nano* **2014**, *8*, 8468–8476. [[CrossRef](#)] [[PubMed](#)]
114. Wang, K.; Zhou, C.; Xi, D.; Shi, Z.; He, C.; Xia, H.; Liu, G.; Qiao, G. Component-Controllable Synthesis of $Co(S_xSe_{1-x})_2$ Nanowires Supported by Carbon Fiber Paper as High-Performance Electrode for Hydrogen Evolution Reaction. *Nano Energy* **2015**, *18*, 1–11. [[CrossRef](#)]
115. Ma, X.; Ma, M.; Liu, D.; Hao, S.; Qu, F.; Du, G.; Asiri, A.M.; Sun, X. Core-Shell-Structured $NiS_2@Ni-Bi$ Nanoarray for Efficient Water Oxidation at Near-Neutral pH. *ChemCatChem* **2017**, *9*, 3138–3143. [[CrossRef](#)]
116. Zeng, L.; Sun, K.; Chen, Y.; Liu, Z.; Chen, Y.; Pan, Y.; Zhao, R.; Liu, Y.; Liu, C. Neutral-pH Overall Water Splitting Catalyzed Efficiently by a Hollow and Porous Structured Ternary Nickel Sulfoselenide Electrocatalyst. *J. Mater. Chem. A* **2019**, *7*, 16793–16802. [[CrossRef](#)]
117. Anjum, M.A.R.; Lee, J.S. Sulfur and Nitrogen Dual-Doped Molybdenum Phosphide Nanocrystallites as an Active and Stable Hydrogen Evolution Reaction Electrocatalyst in Acidic and Alkaline Media. *ACS Catal.* **2017**, *7*, 3030–3038. [[CrossRef](#)]
118. Wang, R.; Dong, X.Y.; Du, J.; Zhao, J.Y.; Zang, S.Q. MOF-Derived Bifunctional Cu_3P Nanoparticles Coated by a N,P-Codoped Carbon Shell for Hydrogen Evolution and Oxygen Reduction. *Adv. Mater.* **2018**, *30*, 1–10.
119. Du, J.; Wang, R.; Lv, Y.R.; Wei, Y.L.; Zang, S.Q. One-Step MOF-Derived Co/Co_9S_8 Nanoparticles Embedded in Nitrogen, Sulfur and Oxygen Ternary-Doped Porous Carbon: An Efficient Electrocatalyst for Overall Water Splitting. *Chem. Commun.* **2019**, *55*, 3203–3206. [[CrossRef](#)]
120. Li, S.; Xi, C.; Jin, Y.Z.; Wu, D.; Wang, J.Q.; Liu, T.; Wang, H.B.; Dong, C.K.; Liu, H.; Kulinich, S.A.; et al. Ir-O-V Catalytic Group in Ir-Doped $NiV(OH)_2$ for Overall Water Splitting. *ACS Energy Lett.* **2019**, *4*, 1823–1829. [[CrossRef](#)]
121. Wu, Z.; Zou, Z.; Huang, J.; Gao, F. $NiFe_2O_4$ Nanoparticles/ $NiFe$ Layered Double-Hydroxide Nanosheet Heterostructure Array for Efficient Overall Water Splitting at Large Current Densities. *ACS Appl. Mater. Interfaces* **2018**, *10*, 26283–26292. [[CrossRef](#)] [[PubMed](#)]
122. Liu, J.; Wang, J.; Zhang, B.; Ruan, Y.; Lv, L.; Ji, X.; Xu, K.; Miao, L.; Jiang, J. Hierarchical $NiCo_2S_4@NiFe$ LDH Heterostructures Supported on Nickel Foam for Enhanced Overall-Water-Splitting Activity. *ACS Appl. Mater. Interfaces* **2017**, *9*, 15364–15372. [[CrossRef](#)]
123. Zhang, Y.; Shao, Q.; Pi, Y.; Guo, J.; Huang, X. A Cost-Efficient Bifunctional Ultrathin Nanosheets Array for Electrochemical Overall Water Splitting. *Small* **2017**, *13*, 1–7. [[CrossRef](#)]
124. Jiang, J.; Sun, F.; Zhou, S.; Hu, W.; Zhang, H.; Dong, J.; Jiang, Z.; Zhao, J.; Li, J.; Yan, W.; et al. Atomic-Level Insight into Super-Efficient Electrocatalytic Oxygen Evolution on Iron and Vanadium Co-Doped Nickel (oxy)hydroxide. *Nat. Commun.* **2018**, *9*, 1–12. [[CrossRef](#)] [[PubMed](#)]
125. Fan, K.; Chen, H.; Ji, Y.; Huang, H.; Claesson, P.M.; Daniel, Q.; Philippe, B.; Rensmo, H.; Li, F.; Luo, Y.; et al. Nickel-Vanadium Monolayer Double Hydroxide for Efficient Electrochemical Water Oxidation. *Nat. Commun.* **2016**, *7*, 1–9. [[CrossRef](#)]
126. Dinh, K.N.; Zheng, P.; Dai, Z.; Zhang, Y.; Dangol, R.; Zheng, Y.; Li, B.; Zong, Y.; Yan, Q. Ultrathin Porous $NiFeV$ Ternary Layer Hydroxide Nanosheets as a Highly Efficient Bifunctional Electrocatalyst for Overall Water Splitting. *Small* **2018**, *14*, 1–9. [[CrossRef](#)] [[PubMed](#)]
127. Stevens, M.B.; Trang, C.D.M.; Enman, L.J.; Deng, J.; Boettcher, S.W. Reactive Fe-Sites in Ni/Fe (Oxy)hydroxide Are Responsible for Exceptional Oxygen Electrocatalysis Activity. *J. Am. Chem. Soc.* **2017**, *139*, 11361–11364. [[CrossRef](#)]
128. Stevens, M.B.; Enman, L.J.; Batchellor, A.S.; Cosby, M.R.; Vise, A.E.; Trang, C.D.M.; Boettcher, S.W. Measurement Techniques for the Study of Thin Film Heterogeneous Water Oxidation Electrocatalysts. *Chem. Mater.* **2017**, *29*, 120–140. [[CrossRef](#)]
129. Trotochaud, L.; Young, S.L.; Ranney, J.K.; Boettcher, S.W. Nickel-Iron Oxyhydroxide Oxygen-Evolution Electrocatalysts: The Role of Intentional and Incidental Iron Incorporation. *J. Am. Chem. Soc.* **2014**, *136*, 6744–6753. [[CrossRef](#)]

130. Zeng, L.; Sun, K.; Yang, Z.; Xie, S.; Chen, Y.; Liu, Z.; Liu, Y.; Zhao, J.; Liu, Y.; Liu, C. Tunable 3D Hierarchical Ni₃S₂ Superstructures as Efficient and Stable Bifunctional Electrocatalysts for both H₂ and O₂ Generation. *J. Mater. Chem. A* **2018**, *6*, 4485–4493. [[CrossRef](#)]
131. Wu, Y.; Li, G.D.; Liu, Y.; Yang, L.; Lian, X.; Asefa, T.; Zou, X. Overall Water Splitting Catalyzed Efficiently by an Ultrathin Nanosheet-Built, Hollow Ni₃S₂-Based Electrocatalyst. *Adv. Funct. Mater.* **2016**, *26*, 4839–4847. [[CrossRef](#)]
132. Yang, Y.; Zhang, K.; Lin, H.; Li, X.; Chan, H.C.; Yang, L.; Gao, Q. MoS₂-Ni₃S₂ Heteronanorods as Efficient and Stable Bifunctional Electrocatalysts for Overall Water Splitting. *ACS Catal.* **2017**, *7*, 2357–2366. [[CrossRef](#)]
133. Yan, Y.; Xia, B.Y.; Zhao, B.; Wang, X. A Review on Noble-Metal-Free Bifunctional Heterogeneous Catalysts for Overall Electrochemical Water Splitting. *J. Mater. Chem. A* **2016**, *4*, 17587–17603. [[CrossRef](#)]
134. Zhou, W.; Wu, X.J.; Cao, X.; Huang, X.; Tan, C.; Tian, J.; Liu, H.; Wang, J.; Zhang, H. Ni₃S₂ Nanorods/Ni Foam Composite Electrode with Low Overpotential for Electrocatalytic Oxygen Evolution. *Energy Environ. Sci.* **2013**, *6*, 2921–2924. [[CrossRef](#)]
135. Feng, J.X.; Xu, H.; Dong, Y.T.; Ye, S.H.; Tong, Y.X.; Li, G.R. FeOOH/Co/FeOOH Hybrid Nanotube Arrays as High-Performance Electrocatalysts for the Oxygen Evolution Reaction. *Angew. Chem. Int. Ed.* **2016**, *55*, 3694–3698. [[CrossRef](#)] [[PubMed](#)]
136. Yu, Z.Y.; Duan, Y.; Gao, M.R.; Lang, C.C.; Zheng, Y.R.; Yu, S.H. A One-Dimensional Porous Carbon-Supported Ni/Mo₂C Dual Catalyst for Efficient Water Splitting. *Chem. Sci.* **2017**, *8*, 968–973. [[CrossRef](#)] [[PubMed](#)]
137. Zhuang, Z.; Sheng, W.; Yan, Y. Synthesis of Monodisperse Au@Co₃O₄ Core-Shell Nanocrystals and Their Enhanced Catalytic Activity for Oxygen Evolution Reaction. *Adv. Mater.* **2014**, *26*, 3950–3955. [[CrossRef](#)]
138. Song, F.; Hu, X. Exfoliation of Layered Double Hydroxides for Enhanced Oxygen Evolution Catalysis. *Nat. Commun.* **2014**, *5*, 1–9. [[CrossRef](#)]
139. Tian, J.; Cheng, N.; Liu, Q.; Sun, X.; He, Y.; Asiri, A.M. Self-Supported NiMo Hollow Nanorod Array: An Efficient 3D Bifunctional Catalytic Electrode for Overall Water Splitting. *J. Mater. Chem. A* **2015**, *3*, 20056–20059. [[CrossRef](#)]
140. Zhang, C.; Zhao, J.; Zhou, L.; Li, Z.; Shao, M.; Wei, M. Layer-by-Layer Assembly of Exfoliated Layered Double Hydroxide Nanosheets for Enhanced Electrochemical Oxidation of Water. *J. Mater. Chem. A* **2016**, *4*, 11516–11523. [[CrossRef](#)]
141. Li, P.; Jin, Z.; Wang, R.; Jin, Y.; Xiao, D. Three-Dimensional Flexible Electrode Derived from Low-Cost Nickel-Phytate with Improved Electrochemical Performance. *J. Mater. Chem. A* **2016**, *4*, 9486–9495. [[CrossRef](#)]
142. Xia, C.; Jiang, Q.; Zhao, C.; Hedhili, M.N.; Alshareef, H.N. Selenide-Based Electrocatalysts and Scaffolds for Water Oxidation Applications. *Adv. Mater.* **2016**, *28*, 77–85. [[CrossRef](#)] [[PubMed](#)]
143. Xiao, C.; Li, Y.; Lu, X.; Zhao, C. Bifunctional Porous NiFe/NiCo₂O₄/Ni Foam Electrodes with Triple Hierarchy and Double Synergies for Efficient Whole Cell Water Splitting. *Adv. Funct. Mater.* **2016**, *26*, 3515–3523. [[CrossRef](#)]
144. Hou, Y.; Lohe, M.R.; Zhang, J.; Liu, S.; Zhuang, X.; Feng, X. Vertically Oriented Cobalt Selenide/NiFe Layered-Double-Hydroxide Nanosheets Supported on Exfoliated Graphene Foil: An Efficient 3D Electrode for Overall Water Splitting. *Energy Environ. Sci.* **2016**, *9*, 478–483. [[CrossRef](#)]
145. Liu, T.; Asiri, A.M.; Sun, X. Electrodeposited Co-Doped NiSe₂ Nanoparticles Film: A Good Electrocatalyst for Efficient Water Splitting. *Nanoscale* **2016**, *8*, 3911–3915. [[CrossRef](#)]
146. Yan, X.; Li, K.; Lyu, L.; Song, F.; He, J.; Niu, D.; Liu, L.; Hu, X.; Chen, X. From Water Oxidation to Reduction: Transformation from Ni_xCo_{3-x}O₄ Nanowires to NiCo/NiCoO_x Heterostructures. *ACS Appl. Mater. Interfaces* **2016**, *8*, 3208–3214. [[CrossRef](#)]
147. Liu, D.; Lu, Q.; Luo, Y.; Sun, X.; Asiri, A.M. NiCo₂S₄ Nanowires Array as an Efficient Bifunctional Electrocatalyst for Full Water Splitting with Superior Activity. *Nanoscale* **2015**, *7*, 15122–15126. [[CrossRef](#)]
148. Yu, Y.; Li, P.; Wang, X.; Gao, W.; Shen, Z.; Zhu, Y.; Yang, S.; Song, W.; Ding, K. Vanadium Nanobelts Coated Nickel Foam 3D Bifunctional Electrode with Excellent Catalytic Activity and Stability for Water Electrolysis. *Nanoscale* **2016**, *8*, 10731–10738. [[CrossRef](#)]
149. Jiang, J.; Gao, M.; Sheng, W.; Yan, Y. Hollow Chevrel-Phase NiMo₃S₄ for Hydrogen Evolution in Alkaline Electrolytes. *Angew. Chem. Int. Ed.* **2016**, *55*, 15240–15245. [[CrossRef](#)]
150. Fang, M.; Gao, W.; Dong, G.; Xia, Z.; Yip, S.P.; Qin, Y.; Qu, Y.; Ho, J.C. Hierarchical NiMo-Based 3D Electrocatalysts for Highly-Efficient Hydrogen Evolution in Alkaline Conditions. *Nano Energy* **2016**, *27*, 247–254. [[CrossRef](#)]

151. Wang, T.; Wang, X.; Liu, Y.; Zheng, J.; Li, X. A Highly Efficient and Stable Biphasic Nanocrystalline Ni-Mo-N Catalyst for Hydrogen Evolution in both Acidic and Alkaline Electrolytes. *Nano Energy* **2016**, *22*, 111–119. [[CrossRef](#)]
152. Xu, K.; Chen, P.; Li, X.; Tong, Y.; Ding, H.; Wu, X.; Chu, W.; Peng, Z.; Wu, C.; Xie, Y. Metallic Nickel Nitride Nanosheets Realizing Enhanced Electrochemical Water Oxidation. *J. Am. Chem. Soc.* **2015**, *137*, 4119–4125. [[CrossRef](#)] [[PubMed](#)]
153. Nandi, S.; Singh, S.K.; Mullangi, D.; Illathvalappil, R.; George, L.; Vinod, C.P.; Kurungot, S.; Vaidhyanathan, R. Low Band Gap Benzimidazole COF Supported Ni₃N as Highly Active OER Catalyst. *Adv. Energy Mater.* **2016**, *6*, 1–11. [[CrossRef](#)]
154. Masa, J.; Sinev, I.; Mistry, H.; Ventosa, E.; De La Mata, M.; Arbiol, J.; Muhler, M.; Roldan Cuenya, B.; Schuhmann, W. Ultrathin High Surface Area Nickel Boride (Ni_xB) Nanosheets as Highly Efficient Electrocatalyst for Oxygen Evolution. *Adv. Energy Mater.* **2017**, *7*, 1–8. [[CrossRef](#)]
155. Yang, C.; Gao, M.Y.; Zhang, Q.B.; Zeng, J.R.; Li, X.T.; Abbott, A.P. In-Situ Activation of Self-Supported 3D Hierarchically Porous Ni₃S₂ Films Grown on Nanoporous Copper as Excellent pH-Universal Electrocatalysts for Hydrogen Evolution Reaction. *Nano Energy* **2017**, *36*, 85–94. [[CrossRef](#)]
156. Wu, A.; Xie, Y.; Ma, H.; Tian, C.; Gu, Y.; Yan, H.; Zhang, X.; Yang, G.; Fu, H. Integrating the Active OER and HER Components as the Heterostructures for the Efficient Overall Water Splitting. *Nano Energy* **2018**, *44*, 353–363. [[CrossRef](#)]
157. Ouyang, B.; Zhang, Y.; Zhang, Z.; Fan, H.J.; Rawat, R.S. Nitrogen-Plasma-Activated Hierarchical Nickel Nitride Nanocorals for Energy Applications. *Small* **2017**, *13*, 1–10. [[CrossRef](#)] [[PubMed](#)]
158. Wang, X.R.; Liu, J.Y.; Liu, Z.W.; Wang, W.C.; Luo, J.; Han, X.P.; Du, X.W.; Qiao, S.Z.; Yang, J. Identifying the Key Role of Pyridinic-N–Co Bonding in Synergistic Electrocatalysis for Reversible ORR/OER. *Adv. Mater.* **2018**, *30*, 1–10. [[CrossRef](#)]
159. Lin, Y.; Yang, L.; Zhang, Y.; Jiang, H.; Xiao, Z.; Wu, C.; Zhang, G.; Jiang, J.; Song, L. Defective Carbon–CoP Nanoparticles Hybrids with Interfacial Charges Polarization for Efficient Bifunctional Oxygen Electrocatalysis. *Adv. Energy Mater.* **2018**, *8*, 1–7. [[CrossRef](#)]
160. Liu, Z.Q.; Cheng, H.; Li, N.; Ma, T.Y.; Su, Y.Z. ZnCo₂O₄ Quantum Dots Anchored on Nitrogen-Doped Carbon Nanotubes as Reversible Oxygen Reduction/Evolution Electrocatalysts. *Adv. Mater.* **2016**, *28*, 3777–3784. [[CrossRef](#)]
161. Fu, Y.; Yu, H.Y.; Jiang, C.; Zhang, T.H.; Zhan, R.; Li, X.; Li, J.F.; Tian, J.H.; Yang, R. NiCo Alloy Nanoparticles Decorated on N-Doped Carbon Nanofibers as Highly Active and Durable Oxygen Electrocatalyst. *Adv. Funct. Mater.* **2018**, *28*, 1–10. [[CrossRef](#)]
162. Li, F.L.; Shao, Q.; Huang, X.; Lang, J.P. Nanoscale Trimetallic Metal–Organic Frameworks Enable Efficient Oxygen Evolution Electrocatalysis. *Angew. Chem. Int. Ed.* **2018**, *57*, 1888–1892. [[CrossRef](#)] [[PubMed](#)]
163. Wang, J.; Xu, F.; Jin, H.; Chen, Y.; Wang, Y. Non-Noble Metal-based Carbon Composites in Hydrogen Evolution Reaction: Fundamentals to Applications. *Adv. Mater.* **2017**, *29*, 1605838–1605872. [[CrossRef](#)]
164. Yu, L.; Xia, B.Y.; Wang, X.; Lou, X.W. General Formation of M-MoS₃ (M = Co, Ni) Hollow Structures with Enhanced Electrocatalytic Activity for Hydrogen Evolution. *Adv. Mater.* **2016**, *28*, 92–97. [[CrossRef](#)] [[PubMed](#)]
165. Li, G.; Yu, J.; Jia, J.; Yang, L.; Zhao, L.; Zhou, W.; Liu, H. Cobalt–Cobalt Phosphide Nanoparticles@Nitrogen-Phosphorus Doped Carbon/Graphene Derived from Cobalt Ions Adsorbed Saccharomycete Yeasts as an Efficient, Stable, and Large-Current-Density Electrode for Hydrogen Evolution Reactions. *Adv. Funct. Mater.* **2018**, *28*, 1–9. [[CrossRef](#)]
166. Najafi, L.; Bellani, S.; Oropesa-Nuñez, R.; Ansaldo, A.; Prato, M.; Del Rio Castillo, A.E.; Bonaccorso, F. Engineered MoSe₂-Based Heterostructures for Efficient Electrochemical Hydrogen Evolution Reaction. *Adv. Energy Mater.* **2018**, *8*, 1–16. [[CrossRef](#)]
167. Yun, Q.; Lu, Q.; Zhang, X.; Tan, C.; Zhang, H. Dreidimensionale Architekturen aus Übergangsmetall-Dichalkogenid-Nanomaterialien zur elektrochemischen Energiespeicherung und -umwandlung. *Angew. Chem.* **2018**, *130*, 634–655. [[CrossRef](#)]
168. Ouyang, T.; Chen, A.N.; He, Z.Z.; Liu, Z.Q.; Tong, Y. Rational Design of Atomically Dispersed Nickel Active Sites in β-Mo₂C for the Hydrogen Evolution Reaction at all pH Values. *Chem. Commun.* **2018**, *54*, 9901–9904. [[CrossRef](#)]

169. Cheng, H.; Ding, L.X.; Chen, G.F.; Zhang, L.; Xue, J.; Wang, H. Molybdenum Carbide Nanodots Enable Efficient Electrocatalytic Nitrogen Fixation under Ambient Conditions. *Adv. Mater.* **2018**, *30*, 1–7. [[CrossRef](#)]
170. Ouyang, T.; Ye, Y.Q.; Wu, C.Y.; Xiao, K.; Liu, Z.Q. Heterostructures Composed of N-Doped Carbon Nanotubes Encapsulating Cobalt and β -Mo₂C Nanoparticles as Bifunctional Electrodes for Water Splitting. *Angew. Chem. Int. Ed.* **2019**, *58*, 4923–4928. [[CrossRef](#)]
171. Freunberger, S.A.; Chen, Y.; Drewett, N.E.; Hardwick, L.J.; Bardé, F.; Bruce, P.G. The Lithium-Oxygen Battery with Ether-Based Electrolytes. *Angew. Chem. Int. Ed.* **2011**, *50*, 8609–8613. [[CrossRef](#)]
172. Freunberger, S.A.; Chen, Y.; Peng, Z.; Griffin, J.M.; Hardwick, L.J.; Bardé, F.; Novák, P.; Bruce, P.G. Reactions in the Rechargeable Lithium-O₂ Battery with Alkyl Carbonate Electrolytes. *J. Am. Chem. Soc.* **2011**, *133*, 8040–8047. [[CrossRef](#)] [[PubMed](#)]
173. Chen, Y.; Freunberger, S.A.; Peng, Z.; Bardé, F.; Bruce, P.G. Li-O₂ Battery with a Dimethylformamide Electrolyte. *J. Am. Chem. Soc.* **2012**, *134*, 7952–7957. [[CrossRef](#)] [[PubMed](#)]
174. McCloskey, B.D.; Speidel, A.; Scheffler, R.; Miller, D.C.; Viswanathan, V.; Hummelshøj, J.S.; Nørskov, J.K.; Luntz, A.C. Twin Problems of Interfacial Carbonate Formation in Nonaqueous Li-O₂ Batteries. *J. Phys. Chem. Lett.* **2012**, *3*, 997–1001. [[CrossRef](#)]
175. Gallant, B.M.; Mitchell, R.R.; Kwabi, D.G.; Zhou, J.; Zuin, L.; Thompson, C.V.; Shao-Horn, Y. Chemical and Morphological Changes of Li-O₂ Battery Electrodes upon Cycling. *J. Phys. Chem. C* **2012**, *116*, 20800–20805. [[CrossRef](#)]
176. Grande, L.; Paillard, E.; Hassoun, J.; Park, J.B.; Lee, Y.J.; Sun, Y.K.; Passerini, S.; Scrosati, B. The Lithium/Air Battery: Still an Emerging System or a Practical Reality? *Adv. Mater.* **2015**, *27*, 784–800. [[CrossRef](#)]
177. Kim, B.G.; Kim, H.J.; Back, S.; Nam, K.W.; Jung, Y.; Han, Y.K.; Choi, J.W. Improved Reversibility in Lithium-Oxygen Battery: Understanding Elementary Reactions and Surface Charge Engineering of Metal Alloy Catalyst. *Sci. Rep.* **2015**, *4*, 18–21. [[CrossRef](#)]
178. Sun, B.; Huang, X.; Chen, S.; Munroe, P.; Wang, G. Porous Graphene Nanoarchitectures: An Efficient Catalyst for Low Charge-Overpotential, Long Life, and High Capacity Lithium-Oxygen Batteries. *Nano Lett.* **2014**, *14*, 3145–3152. [[CrossRef](#)]
179. Ottakam Thotiyl, M.M.; Freunberger, S.A.; Peng, Z.; Chen, Y.; Liu, Z.; Bruce, P.G. A Stable Cathode for the Aprotic Li-O₂ Battery. *Nat. Mater.* **2013**, *12*, 1050–1056. [[CrossRef](#)]
180. Lu, Y.C.; Xu, Z.; Gasteiger, H.A.; Chen, S.; Hamad-Schifferli, K.; Shao-Horn, Y. Platinum-Gold Nanoparticles: A Highly Active Bifunctional Electrocatalyst for Rechargeable Lithium-Air Batteries. *J. Am. Chem. Soc.* **2010**, *132*, 12170–12171. [[CrossRef](#)]
181. Li, F.; Tang, D.M.; Zhang, T.; Liao, K.; He, P.; Golberg, D.; Yamada, A.; Zhou, H. Superior Performance of a Li-O₂ Battery with Metallic RuO₂ Hollow Spheres as the Carbon-Free Cathode. *Adv. Energy Mater.* **2015**, *5*, 1–6. [[CrossRef](#)]
182. Yang, X.H.; He, P.; Xia, Y.Y. Preparation of Mesocellular Carbon Foam and Its Application for Lithium/Oxygen Battery. *Electrochem. Commun.* **2009**, *11*, 1127–1130. [[CrossRef](#)]
183. Read, J. Characterization of the Lithium/Oxygen Organic Electrolyte Battery. *J. Electrochem. Soc.* **2002**, *149*, A1190–A1195. [[CrossRef](#)]
184. Zhang, J.G.; Xiao, J.; Xu, W. Primary Lithium Air Batteries. In *The Lithium Air Battery: Fundamentals*; Springer: New York, NY, USA, 2014; pp. 225–289.
185. Chen, Y.; Freunberger, S.A.; Peng, Z.; Fontaine, O.; Bruce, P.G. Charging a Li-O₂ Battery Using a Redox Mediator. *Nat. Chem.* **2013**, *5*, 489–494. [[CrossRef](#)] [[PubMed](#)]
186. Lacey, M.J.; Frith, J.T.; Owen, J.R. A Redox Shuttle to Facilitate Oxygen Reduction in the Lithium Air Battery. *Electrochem. Commun.* **2013**, *26*, 74–76. [[CrossRef](#)]
187. Bergner, B.J.; Schürmann, A.; Peppler, K.; Garsuch, A.; Janek, J. TEMPO: A Mobile Catalyst for Rechargeable Li-O₂ Batteries. *J. Am. Chem. Soc.* **2014**, *136*, 15054–15064. [[CrossRef](#)] [[PubMed](#)]
188. Lim, H.D.; Song, H.; Kim, J.; Gwon, H.; Bae, Y.; Park, K.Y.; Hong, J.; Kim, H.; Kim, T.; Kim, Y.H.; et al. Superior Rechargeability and Efficiency of Lithium-Oxygen Batteries: Hierarchical Air Electrode Architecture Combined with a Soluble Catalyst. *Angew. Chem. Int. Ed.* **2014**, *53*, 3926–3931. [[CrossRef](#)]
189. Sun, D.; Shen, Y.; Zhang, W.; Yu, L.; Yi, Z.; Yin, W.; Wang, D.; Huang, Y.; Wang, J.; Wang, D.; et al. A Solution-Phase Bifunctional Catalyst for Lithium-Oxygen Batteries. *J. Am. Chem. Soc.* **2014**, *136*, 8941–8946. [[CrossRef](#)]

190. Bergner, B.J.; Hofmann, C.; Schürmann, A.; Schröder, D.; Peppler, K.; Schreiner, P.R.; Janek, J. Understanding the Fundamentals of Redox Mediators in Li-O₂ batteries: A Case Study on Nitroxides. *Phys. Chem. Chem. Phys.* **2015**, *17*, 31769–31779. [[CrossRef](#)]
191. Kwak, W.J.; Hirshberg, D.; Sharon, D.; Shin, H.J.; Afri, M.; Park, J.B.; Garsuch, A.; Chesneau, F.F.; Frimer, A.A.; Aurbach, D.; et al. Understanding the Behavior of Li-Oxygen Cells Containing LiI. *J. Mater. Chem. A* **2015**, *3*, 8855–8864. [[CrossRef](#)]
192. Kundu, D.; Black, R.; Adams, B.; Nazar, L.F. A Highly Active Low Voltage Redox Mediator for Enhanced Rechargeability of Lithium-Oxygen Batteries. *ACS Cent. Sci.* **2015**, *1*, 510–515. [[CrossRef](#)] [[PubMed](#)]
193. Pan, F.; Yang, J.; Huang, Q.; Wang, X.; Huang, H.; Wang, Q. Redox Targeting of Anatase TiO₂ for Redox Flow Lithium-Ion Batteries. *Adv. Energy Mater.* **2014**, *4*, 1–7.
194. Huang, Q.; Li, H.; Grätzel, M.; Wang, Q. Reversible Chemical Delithiation/Lithiation of LiFePO₄: Towards a Redox Flow Lithium-Ion Battery. *Phys. Chem. Chem. Phys.* **2013**, *15*, 1793–1797. [[CrossRef](#)]
195. Huang, Q.; Wang, Q. Next-Generation, High-Energy-Density Redox Flow Batteries. *Chempluschem* **2015**, *80*, 312–322. [[CrossRef](#)]
196. Jia, C.; Pan, F.; Zhu, Y.G.; Huang, Q.; Lu, L.; Wang, Q. High-Energy Density Nonaqueous all Redox Flow Lithium Battery Enabled with a Polymeric Membrane. *Sci. Adv.* **2015**, *1*, 1–7. [[CrossRef](#)] [[PubMed](#)]
197. Zhu, Y.G.; Jia, C.; Yang, J.; Pan, F.; Huang, Q.; Wang, Q. Dual Redox Catalysts for Oxygen Reduction and Evolution Reactions: Towards a Redox Flow Li-O₂ Battery. *Chem. Commun.* **2015**, *51*, 9451–9454. [[CrossRef](#)] [[PubMed](#)]
198. Zhu, Y.G.; Wang, X.; Jia, C.; Yang, J.; Wang, Q. Redox-Mediated ORR and OER Reactions: Redox Flow Lithium Oxygen Batteries Enabled with a Pair of Soluble Redox Catalysts. *ACS Catal.* **2016**, *6*, 6191–6197. [[CrossRef](#)]
199. Chen, S.; Duan, J.; Vasileff, A.; Qiao, S.Z. Size Fractionation of Two-Dimensional Sub-Nanometer Thin Manganese Dioxide Crystals towards Superior Urea Electrocatalytic Conversion. *Angew. Chem. Int. Ed.* **2016**, *55*, 3804–3808. [[CrossRef](#)]
200. Muthuchamy, N.; Jang, S.; Park, J.C.; Park, S.; Park, K.H. Bimetallic NiPd Nanoparticle-Incorporated Ordered Mesoporous Carbon as Highly Efficient Electrocatalysts for Hydrogen Production via Overall Urea Electrolysis. *ACS Sustain. Chem. Eng.* **2019**, *7*, 15526–15536. [[CrossRef](#)]



© 2020 by the authors. Licensee MDPI, Basel, Switzerland. This article is an open access article distributed under the terms and conditions of the Creative Commons Attribution (CC BY) license (<http://creativecommons.org/licenses/by/4.0/>).